

JGR Space Physics

RESEARCH ARTICLE

10.1029/2023JA032286

Key Points:

- This work compares the performance of long-term radiation belt simulations using various inputs and boundary conditions
- Using GOES outer boundary condition, the benchmark simulations reproduce the radiation belt dynamics inside L* = 6 observed by Van Allen Probes
- The data-driven OB condition is critical to the model performance, and stronger loss inside the plasmasphere could improve the performance

Correspondence to:

S.-Y. Lee, leesa@cua.edu

Citation:

Lee, S.-Y., Tu, W., Cunningham, G. S., Cowee, M. M., Wang, D., Shprits, Y. Y., et al. (2024). Simulating long-term dynamics of radiation belt electrons using DREAM3D model. *Journal of Geophysical Research: Space Physics*, 129, e2023JA032286. https://doi.org/10.1029/2023JA032286

Received 15 NOV 2023 Accepted 22 JAN 2024

Simulating Long-Term Dynamics of Radiation Belt Electrons Using DREAM3D Model

Sang-Yun Lee^{1,2}, Weichao Tu³, Gregory S. Cunningham⁴, Misa M. Cowee⁴, Dedong Wang⁵, Yuri Y. Shprits^{5,6,7}, Michael G. Henderson⁴, and Geoffrey D. Reeves⁴

¹NASA Goddard Space Flight Center, Greenbelt, MD, USA, ²Department of Physics, Catholic University of America, Washington, DC, USA, ³West Virginia University, Morgantown, WV, USA, ⁴Los Alamos National Laboratory, Los Alamos, NM, USA, ⁵GFZ German Centre for Geosciences, Potsdam, Germany, ⁶Institute of Physics and Astronomy, University of Potsdam, Potsdam, Germany, ⁷University of California Los Angeles, Los Angeles, CA, USA

Abstract We compared the performance of DREAM3D simulations in reproducing the long-term radiation belt dynamics observed by Van Allen Probes over the entire year of 2017 with various boundary conditions (BCs) and model inputs. Specifically, we investigated the effects of three different outer boundary conditions, two different low-energy boundary conditions for seed electrons, four different radial diffusion (RD) coefficients (D_{LL}) , four hiss wave models, and two chorus wave models from the literature. Using the outer boundary condition driven by GOES data, our benchmark simulation generally well reproduces the observed radiation belt dynamics inside $L^* = 6$, with a better model performance at lower μ than higher μ , where μ is the first adiabatic invariant. By varying the boundary conditions and inputs, we find that: (a) The data-driven outer boundary condition is critical to the model performance, while adding in the data-driven seed population doesn't further improve the performance. (b) The model shows comparable performance with D_{II} from Brautigam and Albert (2000, https://doi.org/10.1029/1999ja900344), Ozeke et al. (2014, https://doi.org/10.1002/ 2013ja019204), and Liu et al. (2016, https://doi.org/10.1002/2015g1067398), while with D_{LL} from Ali et al. (2016, https://doi.org/10.1002/2016ja023002) the model shows less RD compared to data. (c) The model performance is similar with data-based hiss models, but the results show faster loss is still needed inside the plasmasphere. (d) The model performs similarly with the two different chorus models, but better capturing the electron enhancement at higher μ using the Wang et al. (2019, https://doi.org/10.1029/2018ja026183) model due to its stronger wave power, since local heating for higher energy electrons is under-reproduced in the current

Plain Language Summary Relativistic electrons in the outer radiation belt are very dynamic involving various acceleration and loss processes under the influence of radial diffusion (RD), hiss, and chorus waves. The physical processes are regarded as diffusive in behavior. The DREAM3D code solves the Fokker-Plank equation to investigate the radiation belt dynamics in the aspect of the diffusive dynamics of electrons. A variety of empirical models and boundary conditions have been developed and included in the simulations in the literature. In this study, we compare the DREAM3D performance in reproducing the observed radiation belt dynamics with various empirical models of the RD coefficients, hiss and chorus wave, and boundary conditions. In conclusion, we find the data-driven outer boundary condition is very important to reproduce the observed radiation belt variations. For the RD coefficients, all D_{LL} exhibit comparable performances while D_{LL} from Ali et al. (2016, https://doi.org/10.1002/2016ja023002) shows slower RD due to its smaller magnitude. All the hiss wave models lead to effective loss inside the plasmasphere, but stronger losses are needed. For the chorus wave models, the two models are comparable with a small difference in model performance due to the different levels of wave power.

1. Introduction

Relativistic electrons in the outer radiation belt are very dynamic due to the balance of various source and loss processes. The physical mechanisms of radial diffusion (RD) and wave-particle interactions with hiss, chorus, and electromagnetic ion cyclotron (EMIC) waves play important roles in the acceleration and loss of the relativistic electrons. It is important to figure out not only the acceleration mechanism from seed electrons to relativistic energies but also losses of electrons. The RD through betatron acceleration and wave-particle resonant interactions between chorus waves and electrons are well-known as the relativistic electron acceleration

© 2024. American Geophysical Union. All Rights Reserved.

LEE ET AL. 1 of 20



mechanisms in the outer radiation belt (e.g., Li & Hudson, 2019; Meredith et al., 2002; Reeves et al., 2003; Ripoll et al., 2020; Selesnick & Blake, 2000; Summers et al., 1998; Thorne, 2010). On the other hand, hiss and electromagnetic ion-cyclotron (EMIC) waves can scatter relativistic electrons and result in their loss into the atmosphere (e.g., Fu et al., 2011; Li & Hudson, 2019; Li et al., 2013; Reeves et al., 2003; Ripoll et al., 2020; Thorne, 2010). Electrons can also be lost to the outer planetary space by a combination of magnetopause shadowing and outward RD (Fu et al., 2011; Li, 2004; Li & Hudson, 2019; Ripoll et al., 2020; Shprits et al., 2006; Wang et al., 2020).

Theoretically, the Fokker-Plank equation can represent the radiation belt dynamics in the context of the diffusive behavior of electrons. Several simulation models have been developed by solving the 3-D Fokker-Plank diffusion equation (e.g., Glauert et al., 2014b; Reeves et al., 2012; Subbotin & Shprits, 2009). The three-dimensional model of Dynamic Radiation Environment Assimilation Model (DREAM3D) is one of the models, which includes RD, pitch-angle diffusion, and momentum diffusion as well as mixed pitch-angle/momentum diffusion as described in the next section (Reeves et al., 2012; Tu et al., 2013, 2014, 2019). Similar diffusion-type global radiation belt models include, for example, Versatile Electron Radiation Belt-3D (VERB-3D) (Drozdov et al., 2015, 2020, 2021; Kim & Shprits, 2013; Kim et al., 2011, 2012, 2020; Shprits et al., 2009; Subbotin & Shprits, 2009) and the British Antarctic Survey Radiation Belt Model (Glauert et al., 2014a, 2014b, 2018), which have been intensively used over the last decade. Another type of radiation belt models includes convection physics in addition to diffusion, such as the Comprehensive Inner Magnetosphere-Ionosphere model, which is a combination of the Comprehensive Ring Current Model and the Radiation Belt Environment model (Fok et al., 2014; Kang et al., 2018), and VERB-4D model (Aseev & Shprits, 2019; Aseev et al., 2016, 2019; Shprits et al., 2015).

Boundary conditions (BCs) are important for the diffusion-type radiation belt models. For the outer boundary condition which is required for RD, models have used data-driven outer boundary conditions from spacecraft observations, such as Combined Release and Radiation Effects Satellite (CRRES) data at $L^* = 5.5$ (Kim et al., 2011; Tu et al., 2013) or $L^* = 6.6$ (Kim et al., 2012), and Van Allen Probes (Van Allen Probes) data at $L^* = 5.5$ (Drozdov et al., 2015, 2017a, 2017b, 2021). These data-driven outer boundary conditions have been shown to play a crucial role in providing external electron sources in the diffusion models as well as losses of electron by rapid dropouts. However, for an intense storm event that is dominant by local acceleration by chorus waves, Tu et al. (2014) successfully reproduced the enhancement of MeV electrons in the heart of the outer radiation belt without a data-driven outer boundary condition, rather with a Neumann type open outer boundary condition. They also demonstrated that a data-driven minimum energy boundary condition is critical to providing seed electrons for local acceleration by chorus waves. The minimum energy boundary condition is set at the energy of 100 keV to supply seed electrons for chorus heating. While, on the other hand, non-data-driven minimum energy boundary conditions have been used in several global diffusion models which show good performance in reproducing the long-term dynamics of radiation belt electrons (e.g., Drozdov et al., 2020; Tu et al., 2014; Wang & Shprits, 2019).

For the input of ultralow frequency (ULF) wave-driven RD, several empirical models for the RD coefficients (D_{LL}) have been developed in the literature. For example, Brautigam and Albert (2000) developed the RD coefficients composed of electrostatic and electromagnetic terms. However, the electromagnetic diffusion coefficients are only based on limited ULF wave magnetic field observations at only two different L-shell (18 days observation at L=4 and 1 month observation at L=6.6). Due to the limitations of spatial and temporal data set, Ozeke et al. (2014) newly developed empirical RD coefficients as a function of Kp and L based on ULF wave observations from GOES, AMPTE and THEMIS satellites as well as ground magnetometer measurements for a wider data coverage. Subsequently, Ali et al. (2016) established empirical RD coefficients based on Van Allen Probes data as a function of Kp and L^* , which differed from other empirical models in that they employed the Roederer L* (Roederer, 1970) rather than L-shell. L* is defined as $L^* = 2\pi k/\Phi R_e$, where k is Earth's magnetic moment and Φ is the third adiabatic invariant. L^* is identical to L-shell by assuming Earth's magnetic field as a dipole field. Ali et al. (2016) used the geometric mean values of ULF waves rather than arithmetic mean values in other works. At the similar time, Liu et al. (2016) developed an electric component of the RD coefficients based on THEMIS data including a dependence on the first adiabatic invariant μ related to electron energy. Drozdov, Shprits, Aseev, et al. (2017) compared the simulation results using the RD coefficients from Ozeke et al. (2014) and Brautigam and Albert (2000) and concluded that the difference in modeled flux was marginal. Wang et al. (2020) performed simulation for four challenge events selected by the Geospace Environment Modeling (GEM) focus group using four different RD coefficients. They found that for three of the four selected events,

LEE ET AL. 2 of 20



simulations using RD coefficients given by Brautigam and Albert (2000) produce best agreement between satellite observations and simulation results at the heart of the radiation belt. More recently, Drozdov et al. (2021) expanded the comparison study including more RD coefficient models, finding comparable simulation results from their 3D diffusion model among using D_{LL} from Brautigam and Albert (2000), Ozeke et al. (2014), and Liu et al. (2016). However, they found using D_{LL} from Ali et al. (2016) leads to limited transport and acceleration of radiation belt electrons due to the relatively low D_{LL} values from that model.

Hiss waves are responsible for the loss of the outer radiation belt electrons by scattering them into the loss cone. Several empirical models have been developed to quantify the electron scattering loss by hiss waves. For example, Shprits et al. (2006) adopted a simple expression of the electron lifetime ($\tau = 5/\text{Kp}$) in their 3D diffusion model and showed a good agreement between their model results and CRRES observations. Additionally, Tu et al. (2013) calculated pitch angle-momentum diffusion coefficients due to hiss waves using statistical hiss wave observations from CRRES. Orlova et al. (2014) employed the linear regression method to calculate the electron lifetime due to hiss waves scattering as a function of electron energy and L for the first time, incorporating the dependence on MLT and Kp from Spasojevic et al. (2015). Agapitov et al. (2020) also developed an electron lifetime model due to hiss for 1 MeV electrons as a function of AE and L^* , further considering the spatiotemporal variations of the electron plasma frequency to gyrofrequency ratio and the hiss wave frequency. And they extended the valid energy range of the model up to 4 MeV by using the methods from Mourenas and Ripoll (2012) and Pinto et al. (2019). Diffusion simulations utilizing these empirical hiss models showed an efficient reduction of electron flux inside the plasmasphere.

Finally, for the input of chorus waves, which are responsible for the local acceleration of electrons to relativistic energy level, Tu et al. (2013) used CRRES statistical data to calculate the pitch angle-momentum diffusion coefficients of electrons due to chorus. And Wang et al. (2019) newly developed an empirical model for both lower and upper band chorus waves based on more than 5 years of Van Allen Probes data as a function of Kp, *L*, MLAT, and MLT. Tu et al. (2013) and Drozdov et al. (2020) showed that the empirical chorus wave model could provide efficient local acceleration of radiation belt electrons, improving the model performance in producing the long-term radiation belt electron dynamics.

Many of the previous studies have shown that empirical model inputs are sufficient to produce the long-term variability of outer belt electrons. However, during intense storms event-specific model inputs could become more important. For example, Tu et al. (2014) used DREAM3D to simulate a strong radiation belt enhancement observed by Van Allen Probes during an intense storm. They found that both event-specific chorus waves and seed electrons (in minimum energy boundary) are critical to reproduce the observed fast and strong enhancement of electrons. For a 2-day intense storm, Olifer et al. (2019) investigated the event-specific D_{LL} based on ULF wave amplitudes observed by THEMIS satellites during the event, and compared that with the empirical D_{LL} from Ozeke et al. (2014). They found the empirical model could underestimate the D_{LL} by a factor of two or more during the main phase.

As discussed above, various types of boundary conditions and model inputs have been implemented in global radiation belt models, and they are important to simulating the observed dynamics of relativistic electrons in the outer radiation belt. However, the effects of these various model inputs and boundary conditions on the model performance haven't been systematically investigated. In this work, we are motivated to study the effects of various model inputs and boundary conditions, including the RD coefficients, hiss and chorus wave models, and the outer boundary and low-energy boundary conditions. Their effects are tested using the DREAM3D model as a part of the ISWAT (International Space Weather Action Teams) benchmarking challenge, which has been proposed to evaluate the performance of various radiation belt models. The target is to simulate the radiation belt dynamics observed by Van Allen Probes over the entire year of 2017 using GOES observations as the outer boundary condition. We participate in the challenge by conducting DREAM3D simulations of the long-term radiation belt dynamics in 2017 as well as investigating the effects of various boundary conditions and model inputs.

The paper is structured as follows. In Section 2, we briefly introduce the DREAM3D model and the various boundary conditions and inputs to be tested in the simulations. Then in Section 3, we present the benchmark simulation results with the RD coefficient from Ozeke et al. (2014), hiss wave model from Orlova et al. (2014), chorus wave model from Wang et al. (2019), and with the outer boundary condition at $L^* = 6$ based on GOES data. We use these settings as the baseline. In Section 4, we changed the input parameters one by one based on the

LEE ET AL. 3 of 20



other input model options, and then compared the difference and evaluated the model performance during the entire year of 2017.

2. Simulation Model and Inputs

2.1. DREAM3D Model

The governing equation of the DREAM3D model is the 3-D Fokker-Planck equation (Schulz & Lanzerotti, 1974; Tu et al., 2013):

$$\frac{\partial f}{\partial t} = \frac{1}{G} \frac{\partial}{\partial \alpha} \left(G D_{\alpha\alpha} \frac{\partial f}{\partial \alpha} \right) + \frac{1}{p^2} \frac{\partial}{\partial p} \left(p^2 D_{pp} \frac{\partial f}{\partial p} \right) + \frac{1}{G} \frac{\partial}{\partial \alpha} \left(G D_{\alpha p} \frac{\partial f}{\partial p} \right)
+ \frac{1}{p^2} \frac{\partial}{\partial p} \left(p^2 D_{p\alpha} \frac{\partial f}{\partial \alpha} \right) + L^2 \frac{\partial}{\partial L} \left(\frac{D_{LL}}{L^2} \frac{\partial f}{\partial L} \right) - \frac{f}{\tau}$$
(1)

where f is the electron phase space density (PSD) as a function of the three adiabatic invariants, μ , K, L^* (written as L in the equation), and time. G is defined as $T(\alpha)\sin(2\alpha)$ where $T(\alpha)$ is the approximate normalized electron bounce period assuming dipole field, equal to $1.38 - 0.32(\sin(\alpha) + \sqrt{\sin(\alpha)})$. α and p is the equatorial pitch angle and the momentum of electron. The electron lifetime, τ , includes the effects of the electron loss by Coulomb collision with the atmosphere (Tu et al., 2013) and the loss outside the last closed drift shell (LCDS) of electrons (Tu et al., 2019). The LCDS is calculated using the neural network method which is efficient for the long-term simulation (Yu et al., 2012). $D_{\alpha\alpha}$, D_{pp} , and $D_{\alpha p} = D_{p\alpha}$) are the bounce and drift-averaged pitch angle, momentum, and mixed pitch angle-momentum diffusion coefficients, respectively. Hiss waves and upper and lower band chorus waves are considered for the pitch angle-momentum diffusion. All the hiss wave models are spatially restricted inside the plasmasphere, and the location of the plasmapause is obtained from Carpenter and Anderson (1992). Although the original model from Carpenter and Anderson (1992) does not specify the plasmapause location in the dusk to midnight sector, we apply the modeled plasmapause location as an average over all local time since DREAM3D is drift-averaged. All the chorus wave models are only included outside the plasmapause in the model. Note that the wave inputs are averaged over all local times since DREAM3D is drift-averaged. All the chorus wave models are considered only out of the plasmapause. D_{LL} is the RD coefficient. To numerically solve the 3D Fokker-Planck equation, it is decoupled into a 1D RD step with a 3-hr timestep and a 2D pitch-angle/ momentum diffusion step with 2.88-min timestep. For all the simulation runs presented in the next section, we have set the L-range from 1 to 6 uniformly sampled with 50 bins (except for two cases shown in Figure 3 which will be discussed therein), the μ -range from 10^{-2} to 10^5 MeV/G geometrically sampled with 200 bins, and the Krange from 10^{-3} to 10^3 G^{1/2} R_E geometrically sampled with 100 bins. In the 2D pitch-angle/momentum diffusion step, the electron energy ranges from 100 keV to 10 MeV uniformly sampled with 400 bins and the pitch angle ranges from 0° to 90° uniformly sampled with 180 bins. The PSD data and the adiabatic invariants from GOES-13 and GOES-15 satellites are calculated using the TS04 field model (Tsyganenko & Sitnov, 2005) and provided by the ISWAT benchmarking challenge group as a common database to be used for the outer boundary condition (details discussed in next section). Electron PSD data from Van Allen Probes also calculated using the TS04 field model based on flux measurements from the Magnetic Electron Ion Spectrometer (MagEIS) and Relativistic Electron Proton Telescope (REPT) instruments and will also be used by our simulations as discussed in the following sections.

2.2. Boundary Conditions

For the simulation runs presented in the following two sections, we have tested three different types of outer boundary conditions. First, a data-driven outer boundary condition at $L^*=6$ calculated using GOES PSD data. Second, a data-driven boundary condition at $L^*=5.5$ calculated using Van Allen Probes PSD data. Third, a Neumann outer boundary condition at $L^*=11$ with $\partial f/\partial L=0$, which corresponds to an open outer boundary not driven by data. For the first two data-driven outer boundary conditions, interpolation over time is performed between the consecutive crossings of the satellite at the chosen $L_{\rm max}$. The PSD at $L_{\rm min}=1$ is set to be 0. We have also applied two types of low-energy boundary conditions (Emin BC) at $E_{\rm min}=100$ keV. The Emin BC could provide seed electrons to be accelerated to higher energy through both inward RD and local heating. The first type is a fixed-value boundary condition for the 2D pitch-angle/momentum diffusion step with its value updated by the

LEE ET AL. 4 of 20



RD step (Tu et al., 2013). While the second type is a data-driven E_{\min} boundary condition obtained from the Van Allen Probes flux data (Tu et al., 2014).

2.3. Input Models of Radial Diffusion Coefficients

Four different empirical models of RD coefficients, D_{LL} , have been tested in our simulations, which were derived based on different data sets of ULF waves. These include Equation 1 $D_{LL}^{Ozeke} = D_{LL}^{E,Ozeke} + D_{LL}^{B,Ozeke}$ from Ozeke et al. (2014), with:

$$D_{LL}^{E,\text{Ozeke}} = 2.16 \times 10^{-8+0.217L+0.461Kp},$$

$$D_{LL}^{B,\text{Ozeke}} = 6.62 \times 10^{-13-0.0327L^2+0.625L-0.0108Kp^2+0.499Kp}.$$
(2)

Equation 2 $D_{LL}^{BA} = D_{LL}^{E,BA} + D_{LL}^{B,BA}$ from Brautigam and Albert (2000), with:

$$D_{LL}^{E,BA} = \frac{1}{4} \left(\frac{c\tilde{E}}{B_0} \right)^2 \left[\frac{T}{1 + (\omega_d T/2)^2} \right] L^6,$$

$$D_{LL}^{B,BA} = 10^{0.506Kp - 9.325} L^{10},$$
(3)

where $\tilde{E} = 0.26 (\text{Kp} - 1) + 0.1 \text{ mV/m}, B_0 = 0.311 \text{ G}, T = 2700 \text{s}$, and ω_d is the electron drift frequency.

Equation 3 $D_{LL}^{\text{Liu}} = D_{LL}^{E,\text{Liu}} + D_{LL}^{B,\text{Ozeke}}$ with $D_{LL}^{E,\text{Liu}}$ from Liu et al. (2016) as:

$$D_{LL}^{E,\text{Liu}} = 1.115 \times 10^{0.281\text{Kp}-6.0} L^{8.184} \mu^{-0.608}, \tag{4}$$

and $D_{LL}^{B,\mathrm{Ozeke}}$ from Ozeke et al. (2014).

Equation 4 $D_{LL}^{Ali} = D_{LL}^{E,Ali} + D_{LL}^{B,Ali}$ from Ali et al. (2016), with:

$$D_{LL}^{E,\text{Ali}} = e^{-16.951 + 0.181 \text{Kp} \cdot L + 1.982L},$$

$$D_{LL}^{B,\text{Ali}} = e^{-16.253 + 0.224 \text{Kp} \cdot L + L}.$$
(5)

All the L parameters in the above D_{LL} models are approximated as L^* in our simulations.

In the original D_{LL} derivations of Fälthammar (1965), the RD coefficients are separated into electrostatic and electromagnetic diffusion coefficients, D_{LL}^E and D_{LL}^B , respectively. Therefore, D_{LL}^E should contain only fluctuations in the electric potential that are not associated with magnetic fluctuations, and D_{LL}^B should contain fluctuations in the magnetic field for which there are induced electric fields. However, the electric field measured by satellites is the total electric field including both the electrostatic and induced electric fields, which is not properly separated in the empirical D_{LL} models due to its complexity. In this reason, the empirical RD coefficients used in this study may be overestimated (Drozdov et al., 2021; Lejosne & Kollmann, 2020; Liu et al., 2016).

Both electric and magnetic RD coefficients depend on particle energy in terms of drift frequency (ω_d) and magnetic moment (μ) (Fei et al., 2006). $D_{LL}^{E,BA}$ contains the drift frequency term in Equation 3, and $D_{LL}^{E,\text{Liu}}$ is calculated by directly fitting the factor μ instead of drift frequency. On the other hand, Ozeke et al. (2014) and Ali et al. (2016) do not consider μ as a factor of RD coefficient. Ozeke et al. (2014) neglect the drift frequency term by assuming that the azimuthal electric field power spectral density in the equatorial plane is independent of frequency. Ali et al. (2016) calculated the distribution of the power spectral density of ULF waves in L^* and frequency and found the azimuthal electric component is independent of frequency while the compressional magnetic component decreases exponentially only at higher frequencies range (f > 4 mHz). However, their RD coefficients based on the spectral distribution are very weakly dependent on the frequency in the domain (3 < L < 5.5, 0 < Kp < 5, and $500 < \mu < 5,000 \text{ MeV/G}$) so that they present their models without μ dependence.

LEE ET AL. 5 of 20



2.4. Input Models of Plasmaspheric Hiss

Four different models for the effects of plasmaspheric hiss have been implemented. First, we have used the hiss model statistically derived from the CRRES wave data and calculated pitch-angle/momentum diffusion coefficients at different electron energies, pitch angle, L, and AE* levels due to hiss (Tu et al., 2013), where AE* is the averaged AE index over the previous 1 hr. Here, we assumed a dipole background magnetic field and adopted the cold electron density model from Carpenter and Anderson (1992). The other three types of hiss effect models directly provide the resulting electron lifetimes due to hiss scattering without solving the 2D pitch-angle/momentum diffusion. These include the lifetime model from Orlova et al. (2014), which used the statistical wave data from the CRRES mission and parameterized the electron loss lifetimes due to hiss as a function of L (approximated as L^* for our simulations), electron energy, and Kp. The second hiss loss lifetime model is from Agapitov et al. (2020), who used the statistical wave data from Van Allen Probes and also parameterized the electron lifetimes as a function of L* (calculated using T89 magnetic field model) and AE. They focused the parameterization on the electron lifetimes at 1 MeV and then expanded the valid energy range to 1 MeV < E < 4 MeV by referring to the previous study (Mourenas & Ripoll, 2012; Pinto et al., 2019). When the Agapitov et al. (2020) hiss model is used in our simulation, it is applied to electron energies over the entire simulation domain. The last hiss loss lifetime model we test here is a simple model with $\tau[day] = 5/Kp$ from Shprits et al. (2006).

2.5. Input Models of Chorus Waves

Finally, we have tested two different types of empirical chorus wave models. The first one is statistically derived from the CRRES wave data (Tu et al., 2013). The second is from Wang et al. (2019) derived from the long-term Van Allen Probes wave observations. Both models provide the power of chorus waves as a function of magnetic local time, latitude, and L, binned at different AE levels in the Tu et al. (2013) model but at different Kp levels in the Wang et al. (2019) model. Based on these statistical wave distributions, we then calculate the 2D pitch-angle/momentum diffusion coefficients due to chorus waves and implement them in DREAM3D simulations. Here, we also assumed a dipole background magnetic field and adopted the cold electron density model from Sheeley et al. (2001) outside the plasmasphere for the diffusion coefficients of chorus waves.

3. Benchmark Simulations

In this section, we present the benchmark simulation results using DREAM3D for the year of 2017, which serves as the baseline to compare with other simulation runs with different boundary conditions and model inputs. Specifically, for this simulation we have used the RD coefficients from Ozeke et al. (2014), the hiss lifetime model from Orlova et al. (2014), and the chorus wave model from Wang et al. (2019), with the outer boundary condition driven by GOES data at $L^* = 6$ and the non-data-driven E_{\min} boundary condition. To better document the inputs combinations used in the benchmark simulations and subsequent simulations discussed in Section 4, in Table 1 we summarize the input selections for all the model runs presented in this paper. The wave inputs for the benchmark simulations are selected since they generally show the best performance among the other combinations which will be discussed in Section 4. The boundary condition selections are motivated by the ISWAT challenge. For the benchmark simulations, we have compared the results with RD only from the data-driven outer boundary (RD only), RD plus hiss wave effects (RD + Hiss), and finally all effects of RD, hiss, and chorus waves (RD + Hiss + Chorus (R + H + C)), which are then compared with the Van Allen Probes observations at two different μ values, 510 MeV/G and 1237 MeV/G respectively, and at K = 0.117 G^{1/2} R_E .

Figure 1a shows the variations of PSD data from both GOES and Van Allen Probes at $\mu=510$ MeV/G, K=0.117 G^{1/2} R_E over the L^* range of 3–6 during the entire year of 2017. The values of the corresponding electron kinetic energy at each L^* are shown on the right y-axis (estimated using the dipole field model). The black solid line shows the location of plasmapause (calculated using the Carpenter and Anderson (1992) model). Figure 1b shows the DREAM3D model result in PSD with only the RD effect using the RD coefficients from Orlova et al. (2014). The data-driven outer boundary condition acts as the external source of electrons which are transported to lower L^* regions through inward RD. In this run, we find the modeled PSDs generally capture the observed electron variation at higher L^* , but highly overestimate the PSD at lower L^* compared to the observations. To quantify the model performance, we have used the metric of median symmetric accuracy (MSA) as a function of L^* defined as (Morley et al., 2018):

LEE ET AL. 6 of 20



 Table 1

 Input Combinations of Each Run Are Described

Run #	Corresponding figure	Outer BC	Emin BC	D_{LL} model	Hiss model	Chorus model
1	Figures 1b and 1g	GOES at $L^* = 6$	Fixed-type	Ozeke et al. (2014)	Off	Off
2	Figures 1c and 1h	GOES at $L^* = 6$	Fixed-type	Ozeke et al. (2014)	Orlova et al. (2014)	Off
3*	Figures 1d and 1i	GOES at $L^* = 6$	Fixed-type	Ozeke et al. (2014)	Orlova et al. (2014)	Tu et al. (2013)
4	Figures 2c and 2j	Van Allen Probe at $L^* = 5.5$	Fixed-type	Ozeke et al. (2014)	Orlova et al. (2014)	Tu et al. (2013)
5	Figures 2d and 2k	Neumann at $L^* = 11$	Fixed-type	Ozeke et al. (2014)	Orlova et al. (2014)	Tu et al. (2013)
6	Figures 2e and 21	Neumann at $L^* = 11$	Van Allen Probes	Ozeke et al. (2014)	Orlova et al. (2014)	Tu et al. (2013)
7	Figures 2f and 2m	GOES at $L^* = 6$	Van Allen Probes	Ozeke et al. (2014)	Orlova et al. (2014)	Tu et al. (2013)
8	Figures 7c and 7k	GOES at $L^* = 6$	Fixed-type	Brautigam and Albert (2000)	Orlova et al. (2014)	Tu et al. (2013)
9	Figures 7d and 7l	GOES at $L^* = 6$	Fixed-type	Liu et al. (2016) & Ozeke et al. (2014)	Orlova et al. (2014)	Off
10	Figures 7e and 7m	GOES at $L^* = 6$	Fixed-type	Ali et al. (2016)	Orlova et al. (2014)	Tu et al. (2013)
11	Figures 7f and 7n	GOES at $L^* = 6$	Fixed-type	Ozeke et al. (2014)	Off	Off
12	Figures 7g and 7o	GOES at $L^* = 6$	Fixed-type	Liu et al. (2016) & Ozeke et al. (2014)	Off	Off
13	Figures 9c and 9i	GOES at $L^* = 6$	Fixed-type	Ozeke et al. (2014)	Agapitov et al. (2020)	Tu et al. (2013)
14	Figures 9d and 9j	GOES at $L^* = 6$	Fixed-type	Ozeke et al. (2014)	Tu et al. (2013)	Tu et al. (2013)
15	Figures 9e and 9k	GOES at $L^* = 6$	Fixed-type	Ozeke et al. (2014)	Shprits et al. (2006)	Tu et al. (2013)
16	Figures 11c and 11g	GOES at $L^* = 6$	Fixed-type	Ozeke et al. (2014)	Orlova et al. (2014)	Wang et al. (2019)

Note. Run #3 with asterisk symbol corresponds to the same panels in Figures 1d and i), Figures 2b and i), Figures 7b and k), Figures 9b and h), and Figures 11b and f) as the benchmark run.

$$MSA(L^*)[\%] = 100 \left(e^{M(|\log_e(m_i/d_i)|)} - 1 \right), \tag{6}$$

where M is a median function over time with index i, and m_i and d_i are arrays of model results and observation data at a given L^* over different times, respectively. MSA is a useful parameter to compare the difference between the model and data of a logarithmic scale and it treats overestimate and underestimate from the model equally. If the model results match the data perfectly, it corresponds to a MSA of 0%. Higher MSA means bigger difference between the model and data, for example, a median difference by a factor of 3 leads to a MSA of $\sim 200\%$ (i.e., the MSA could be approximately considered as the overestimation/underestimation factor). The calculated MSA versus L^* for the RD only run is shown as the red curve in Figure 1e, which shows good performance at large L^* regions with MSA<150% outside $L^* = 4$ and increasing MSA as L^* decreases.

Then the effects of hiss waves are included in the new run shown in Figure 1c, with its MSA versus L^* results shown as the blue curve in Figure 1e. We find that adding in hiss waves effectively scatters the electrons inside the plasmasphere, largely reducing the MSA inside $L^*=4$ (by comparing the blue and red curves in Figure 1e), even though the model still slightly overproduces the PSD at low L^* regions inside the plasmasphere leading to higher MSA there than at high L^* regions. Finally, we add in the chorus waves and the model results including all the effects of RD, hiss wave, and chorus waves are shown in Figure 1d, with its MSA profile overplotted as the black curve in Figure 1e. Counterintuitively, adding in chorus doesn't lead to apparent PSD enhancement at this μ value by comparing Figures 1d to 1c; rather it leads to slight reduction in PSD at both high and low L^* regions for example, during the period of May 1 to Jul 1. Correspondingly, it helps improve the overestimation at low L^* and slightly lowering the MSA at $L^* < 4.2$ as shown by the black curve in Figure 1e compared to the blue curve. These interesting effects from chorus waves at lower μ value could be understood in combination with the results at higher μ value in terms of energy diffusion, which will be discussed below.

With the same configuration of Figures 1a–1e for electrons at a lower μ value, Figures 1f–1j show the model results at higher $\mu = 1237$ MeV/G with the same K value, which corresponds to electrons of higher energies by comparing the right y-axes of Figures 1a and 1f. For the RD only run (Figure 1g), we find that for electrons at higher μ RD is shown to be insufficient in reproducing the electron enhancement at the higher μ value compared to

LEE ET AL. 7 of 20

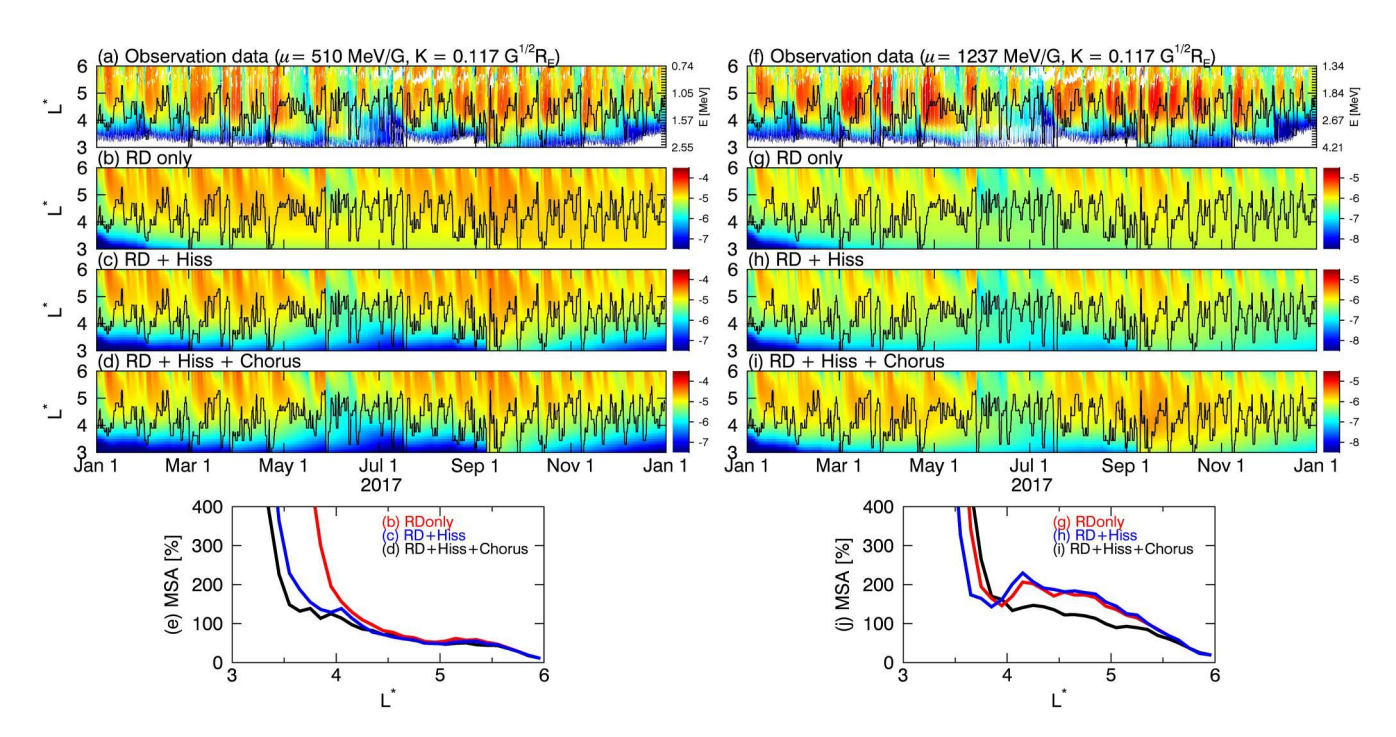


Figure 1. Phase space density (PSD) distribution and error analyses from the benchmark simulations for (a–e) $\mu = 510$ MeV/G and K = 0.117 G^{1/2} R_E and (f–j) $\mu = 1,237$ MeV/G and K = 0.117 G^{1/2} R_E . Panels (a, f) show the observed PSD data from GOES and Van Allen Probes satellites. The black solid lines show the location of plasmapause. Simulated PSD from DREAM3D simulations include results with (b, g) radial diffusion (RD) only, (c, h) RD + Hiss, and (d, i) RD + Hiss + Chorus. Panels (e, j) show the calculated median symmetric accuracy as a function of L^* , with the red lines for RD only, blue lines for RD + Hiss, and black lines for RD + Hiss + Chorus.

the lower μ , which is also suggested by the larger MSA of the RD only run at large L^* values in Figure 1 compared to Figure 1e. For the RD + Hiss run (Figure 1h), similar to the results at the lower μ value on the left, adding in hiss at higher μ leads to electron loss inside the plasmasphere and lower MSA in Figure 1j compared to the RD only run. But the PSD is still overestimated at low L^* values by comparing to the data in Figure 1f, worse than the lower μ case. Then, further including chorus waves for this higher μ case (Figure 1i) provides efficient local heating of electrons, which leads to a clear drop of the MSA in Figure 1j from the blue curve to the black curve at large L^* regions ($L^* > 4$). However, due to the enhanced PSD at high L^* regions from chorus heating and the concurrent inward RD, the modeled PSD also increase at lower L^* regions inside the plasmasphere, resulting in more overestimation at $L^* < 4$ and higher MSA there in the black curve of Figure 1j compared to the blue one. Looking at the chorus heating results at both low and high μ values, we find that interestingly chorus waves slightly reduces the electron PSD for the lower μ case while increase the PSD at higher μ case. To understand these, in Figure 2 we plot the PSD versus μ distributions from the simulations at 3UT of Apr 22 and $L^* = 4.5$ (outside plasmapause at that time) for the same K value as the simulation results shown in Figure 1. The black dashed curve is for the RD + Hiss run without chorus effects and the black solid curve is for the RD + Hiss + Chorus run after adding in the chorus. The results show that the energy diffusion from chorus waves works to smooth out the PSD versus μ distribution from the dashed to the solid black curves. In addition, higher pitch angle diffusion rates at lower energy also contribute to the enhanced loss of electron PSD at lower μ . By taking two cuts at $\mu = 510 \text{ MeV/G}$ (low μ case in Figure 1) and $\mu = 1237 \text{ MeV/G}$ (high μ case) respectively, we find that the chorus waves lead to reduced PSD at low μ from the dashed to the solid black curves and increased PSD at high μ . Therefore, the chorus effects on radiation belt electrons are μ dependent. Finally, by comparing the black curves in Figure 1; versus Figure 1e, we find that the model's overall performance is worse at higher μ than lower μ . The acceleration at large L^* regions is underestimated to a larger degree by the model at higher μ , thus showing slightly higher MSA values at large L^* in the black curve of Figure 1; compared to Figure 1e. These results suggest that stronger chorus heating is needed for higher energy electrons. Other candidate to explain the insufficient acceleration can be related with background plasma density. Allison and Shprits (2021) showed that realistic low plasma density condition is required for the acceleration of multi-MeV electrons.

LEE ET AL. 8 of 20

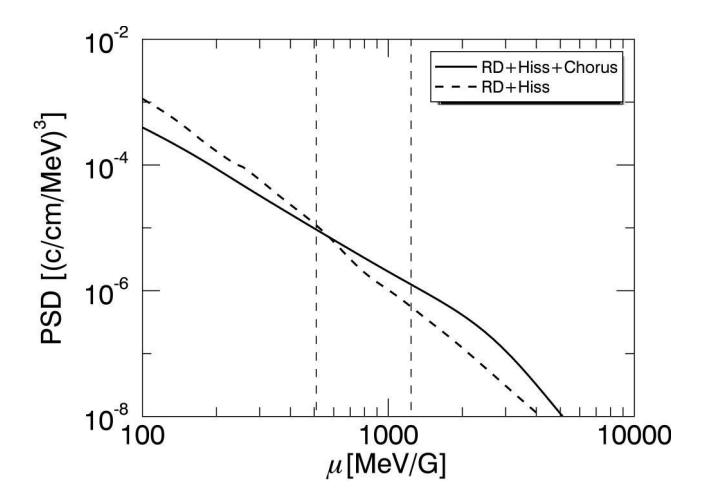


Figure 2. Phase space density distribution as a function of μ with radial diffusion (RD) + Hiss (no chorus waves) in dashed line and RD + Hiss + Chorus in solid line using the chorus wave model from Wang et al. at $K = 0.117 \text{ G}^{1/2}R_E$, $L^* = 4.5$, and 3UT on 22 April 2017. The two vertical dashed lines corresponds to $\mu = 510 \text{ MeV/G}$ and $\mu = 1237 \text{ MeV/G}$ respectively.

Figure 1 shows a model-data comparison in electron PSD at fixed μ and Kvalues. It is also worthwhile to compare the model and data in electron flux at fixed values of electrons energy and pitch angle for the benchmark simulation. Figure 3 compares the observed and simulated electron fluxes of the benchmark simulation (for the run with RD + Hiss + Chorus as shown in Figures 1d and 1i) at two different pairs of electron energies and pitch angles (900 keV, 57.27°) and (1.8 MeV, 58.23°). Again, the model performance is better at lower electron energy (comparing the data shown in Figure 3a and model shown in Figure 3b) than higher energy (comparing Figures 3c and 3d). At electron energy of 1.8 MeV, we see that the electron acceleration at large L^* regions is generally underestimated by the model and the model overestimates the electron flux at low L^* regions. Another feature which is more evident here compared to the PSD plots is that some of the fast dropouts of electron flux in the observations, with examples marked by the red arrows in both Figures 3a and 3c, are not well captured by the model. As a reference, the calculated LCDS of electrons at $K = 0.117 \text{ G}^{1/2}R_E$ is plotted as the red curve in Figures 3a and 3c. Some of observed dropouts occurred when LCDS approached inside $L^* = 6$, some did not. These misses of fast dropouts in the model could be due to the lack of realistic background magnetic field model. Radial diffusion coefficients in a non-dipolar magnetic field are much higher by a few orders of magnitudes near the LCDS during times of high

geomagnetic activity, and would produce more loss (Cunningham, 2016). In addition, the model missed the fast dropout mechanism due to the lack of EMIC waves which could lead to fast loss of energetic electrons. Also the

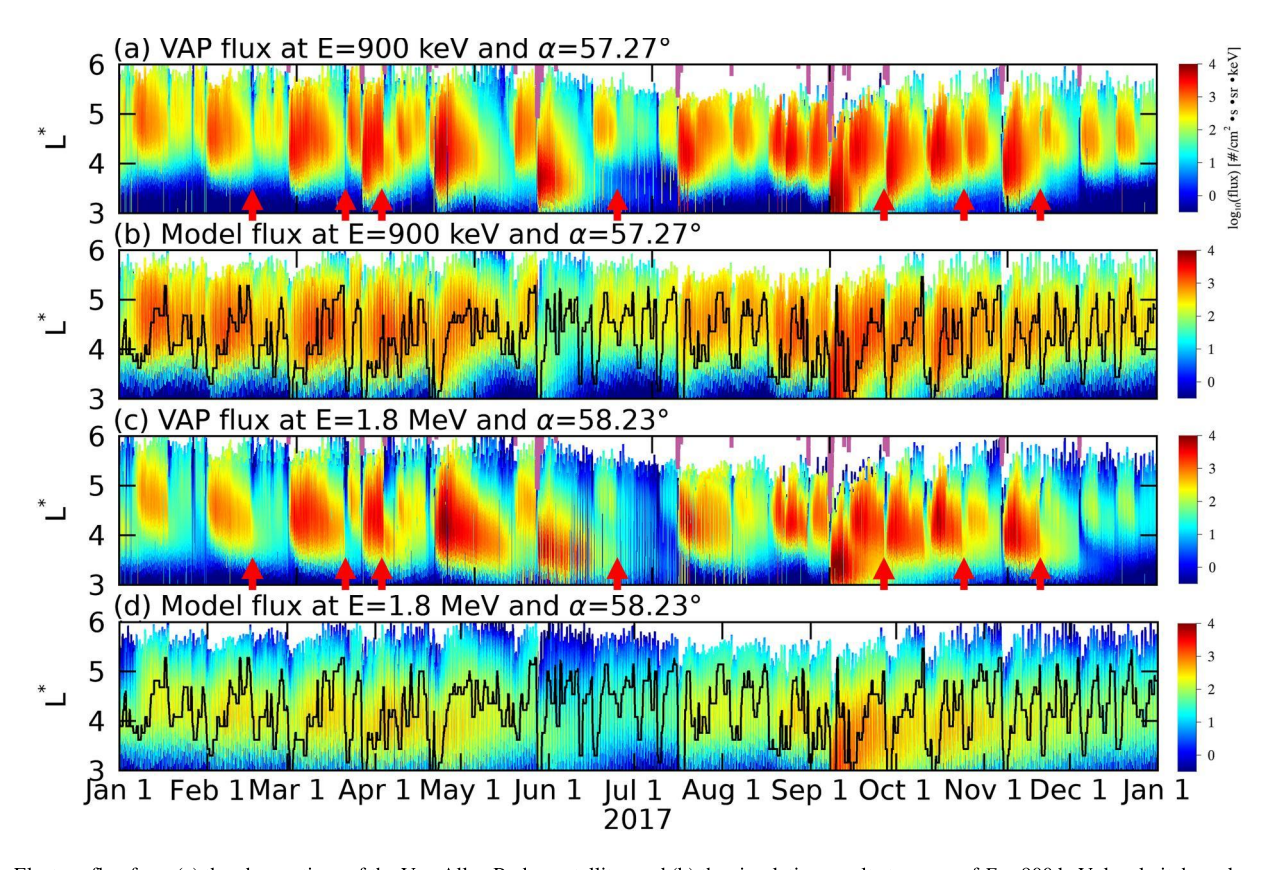


Figure 3. Electron flux from (a) the observations of the Van Allen Probes satellites and (b) the simulation result at energy of E = 900 keV, local pitch angle $\alpha = 57.27^{\circ}$. Panels (c) and (d) show the electron flux of the same format as (a) and (b) but at E = 1.8 MeV, local pitch angle $\alpha = 58.23^{\circ}$. The black solid lines in panels (b) and (d) show the plasmapause location and the light purple solid lines in panels (a) and (c) show the last closed drift shell location. The arrows in panels (b) and (d) mark some examples of fast dropout of electrons.

LEE ET AL. 9 of 20

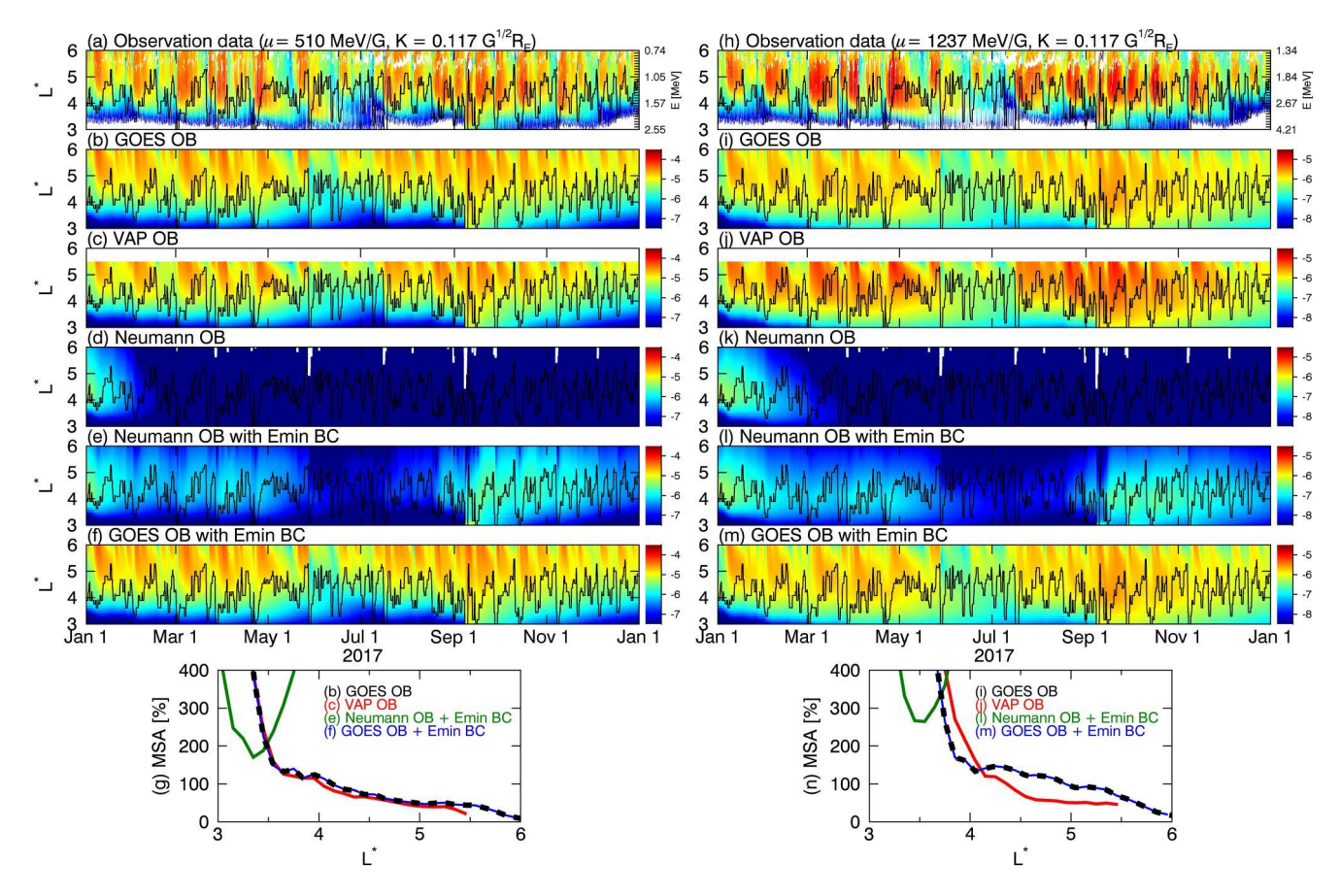


Figure 4. (a, b, i, h): Identical to Figures 1a, 1d, 1f, and 1i, respectively. The remaining spectral plots are simulated phase space density using (c, j) the Van Allen Probes boundary condition at $L^* = 5.5$, (d, k) the Neumann outer boundary condition at $L^* = 11$, (e, l) the Neumann OB and the data-driven minimum energy boundary condition (Emin BC), and (f, m) both GOES Outer BC and Emin BC. The white curves in panels (d) and (k) show the last closed drift shell location. (g, n) The median symmetric accuracy (MSA) distribution as a function of L^* . The cases of the Neumann BC without the Emin BC shown in panels (d, k) are not shown due to their large errors. The black curves and blue curves are overlapped in both MSA plots (g, n), so the black curves are plotted as dashed curves for better visualization.

calculated LCDS using neural network may not be realistic during specific dropout events since the neural network model of LCDS is statistically averaged.

4. Testing Various Boundary Conditions and Model Inputs

To investigate the effects of various boundary conditions and model inputs on the performance of DREAM3D in reproducing the long-term outer belt dynamics, we use the benchmark simulation results presented in Figures 1d and 1i as the baseline and change the major model boundary conditions and inputs one at a time in this section, with results discussed below.

4.1. Outer Boundary Conditions

The outer boundary condition (OB) is an important boundary condition for the DREAM3D model. In this subsection, we tested two types of data-driven boundary conditions and an open Neumann boundary condition. The corresponding results are shown in Figure 4. Figures 4b and 4i are identical to Figures 1d and 1i which are the benchmark simulation results using the OB condition calculated from GOES PSD data when the satellite crosses $L^* = 6$. Between the crossings interpolation is performed over time to fill the gaps. For the results in Figures 4c and 4j, similar calculation is performed to achieve an OB condition at $L^* = 5.5$ using the Van Allen Probes PSD data (and the other model boundary conditions and inputs are identical to the benchmark simulations). This new OB condition is set up at a lower L^* value since, unlike the GOES satellite, the Van Allen Probes satellites generally don't reach $L^* = 6$. Comparing Figure 4b with Figure 4c, we find that the difference in the simulation results between using the GOES OB condition at $L^* = 6$ and using the Van Allen Probes OB condition at $L^* = 5.5$

LEE ET AL. 10 of 20

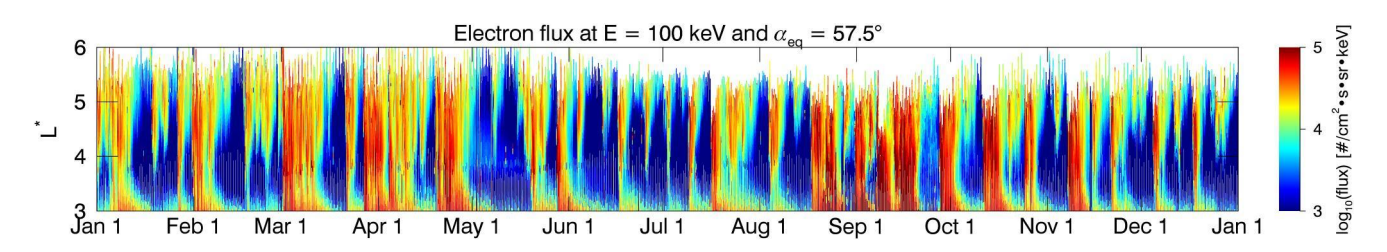


Figure 5. Observed electron flux at E = 100 keV and local pitch angle $\alpha_{local} = 57.5^{\circ}$.

for the lower μ case is not significant. This is also reflected in the MSA results in Figure 4g, which shows that the red curve (Van Allen Probes OB run) is minimally better than the black curve (GOES OB run). Note that the black curve overlaps the blue curve (which will be discussed in the next subsection) so the black curve is plotted as a dashed curve for better visualization. On the other hand, the simulated PSD values at higher $\mu = 1237$ MeV/G are more different between using the GOES OB condition at $L^* = 6$ (Figure 4i) and using the Van Allen Probes OB condition at $L^* = 5.5$ (Figure 4j). Figure 4n shows that at higher μ the run with Van Allen Probes OB (in red) yields lower MSA values outside L^* of 4 compared to the GOES OB run in black (overlapped with blue). This is likely because local heating is more dominant for higher μ electrons than lower μ electrons, as discussed in previous session. For the higher- μ case, the Van Allen Probes OB condition at $L^* = 5.5$ captures more of the local heating in the outer boundary condition itself than the GOES OB condition at $L^* = 6$ since $L^* = 5.5$ is closer to the heart of the outer belt. This leads to better performance of the simulation using the Van Allen Probes OB condition in capturing the electron acceleration in the heart of the outer belt. One other potential reason may be from the data processing. We had to do some assumptions to produce GOES differential data above 1 MeV. It may induce the PSD difference between GOES and Van Allen Probes at L^* from 5 to 6 of Figure 4h.

Next, instead of using data-driven OB conditions, we tested the Neumann boundary condition at $L^* = 11$ which can be regarded as an open boundary condition. The results are plotted in Figures 4d and 4k, which show that the electron PSD from the initial condition quickly decay in time at both μ values. This is due to the lack of the external source from the outer boundary and loss of electrons to the magnetopause (simulated by outward RD and fast loss outside the LCDS which is plotted as the white curves in Figures 4d and 4k) and atmosphere (simulated by pitch angle diffusion by hiss and chorus waves). Also, due to the lack of electron seed population transported inward from the data-driven outer boundary, the acceleration effect of the chorus waves is insufficient to produce local acceleration of electrons. These results suggest that the data-driven outer boundary condition is critical to the performance of the model in reproducing the long-term dynamics of electrons in the outer belt.

4.2. E_{\min} Boundary Conditions

The lack of seed population in the Neumann OB run discussed above motivates us to test the effects of data-driven low energy boundary condition (Emin BC) for the simulations. The Emin BC could provide seed electrons to be accelerated to higher energy through both RD and local heating. The data-driven Emin BC is calculated using Van Allen Probes MagEIS data at the electron energy $E=100~{\rm keV}$ over all local pitch angle ($0 \le \alpha_{\rm local} \le 90^{\circ}$) which are interpolated to cover all the time and L^* grids of the simulations. An example of the observed flux variations at the Emin boundary at a local pitch angle of 57.5° is shown in Figure 5, which show frequent injections of electrons from high L^* into low L^* regions.

The data-driven Emin BC is first implemented into the run with the Neumann OB with results shown in Figures 4e and 4l. By comparing to Figures 4d and 4k for both μ values, we find that the model results with the data-driven Emin BC better produce the variations of PSD. However, overall the simulation results with the Neumann OB and data-driven Emin BC greatly underestimated the observed PSD at high L^* regions, which is also demonstrated by the large MSA values at $L^* > 3.5$ for the lower μ case as shown by the green curve in Figure 4g and at $L^* > 3.7$ for the higher μ case as shown in Figure 4n. Therefore, comparing the model results with data-driven OB only with those with data-driven Emin BC only (e.g., Figure 4b versus 4e), we find that the data-driven OB is more important in capturing the long-term dynamics of radiation belt electrons.

Given that the data-driven Emin BC improves the performance of the simulations with Neumann OB, it is interesting to see if it will help further improve the performance of the simulations with the data-driven OB. The

LEE ET AL. 11 of 20

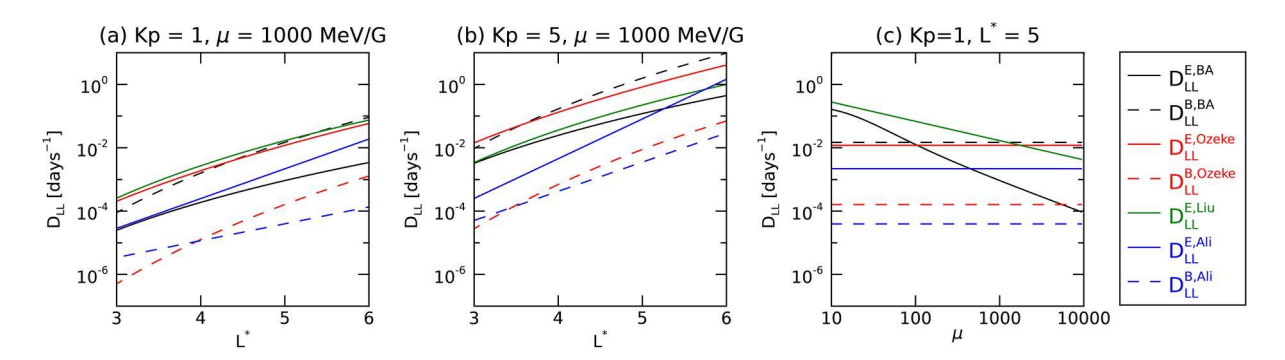


Figure 6. The various radial diffusion coefficients as a function of L^* at $\mu = 1000$ MeV/G for (a) Kp = 1 and (b) Kp = 5. Panel (c) shows D_{LL} as a function of μ at $L^* = 5$ and Kp = 5.

simulation results with both data-driven OB and data-driven Emin BC are shown in Figures 4f and 4m. By comparing to the model results with only data-driven OB in the benchmark runs (Figures 4b and 4i), we find that the modeled PSD show almost no change at these two μ values with the additional data-driven Emin BC, which is also shown in the MSA plots where the blue curves for the new runs with both data-driven OB and Emin BC overlap with the black curves for the benchmark runs. By investigating more μ values (not shown here), we find that enhanced PSD from the data-driven Emin BC is only evident at much lower μ values closer to the Emin boundary, which suggest that the local heating from the empirical chorus model used in our simulations is not fast enough to accelerate the additional seed electrons from the data-driven Emin boundary (100 keV) to MeV range. Therefore, the model results show that adding in data-driven Emin BC on average is not improving the model performance for the long-term simulation given that a data-driven OB is already implemented.

4.3. Radial Diffusion Coefficients

There have been several studies to calculate the RD coefficients (Ali et al., 2016; Brautigam & Albert, 2000; Liu et al., 2016; Ozeke et al., 2014). Wang et al. (2020) and Drozdov et al. (2021) have already compared the model results with the various RD coefficient using the VERB code. However, we test the various RD coefficients using the DREAM3D model here.

Figures 6a and 6b show the magnitudes of both the electric and magnetic RD coefficients from the various D_{IJ} models listed in Section 2 at different Kp values and constant μ . We find that in all the D_{LL} models D_{LL}^E (solid curves) is higher than D_{LL}^{B} (dashed curves), except for the D_{LL}^{BA} model where $D_{LL}^{B,BA}$ is larger than $D_{LL}^{E,BA}$ since $D_{LL}^{B,BA}$ is actually electromagnetic rather than purely magnetic. At Kp = 1, focusing on the dominant component of D_{LL} in each model (the solid curves), we find that $D_{LL}^{B,BA}$, $D_{LL}^{E,Ozeke}$, and $D_{LL}^{E,Liu}$ are comparable, which are higher than $D_{II}^{E,Ali}$ by almost an order of magnitude. This is likely due to the different approaches used to quantify the RD coefficients: Ali et al. (2016) used the geometric mean values of the statistical ULF wave power, which are close to the median values, while the other studies such as Ozeke et al. (2014) and Liu et al. (2016) used the arithmetic mean values. At higher Kp = 5, all the RD coefficients are enhanced, and we found a rough relation that $D_{LL}^{B,BA} > D_{LL}^{E,Ozeke} > D_{LL}^{E,Liu} > D_{LL}^{E,Ali}$. Furthermore, $D_{LL}^{E,Liu}$ and $D_{LL}^{E,BA}$ are μ -dependent, while the other D_{LL} models do not depend on μ . Figure 6c shows the RD coefficients as a function of μ at the constant values of Kp = 5 and $L^* = 5$. We find that $D_{LL}^{E, \text{Liu}}$ (green line) is the largest for smaller μ , which decreases in μ so that it becomes smaller than $D_{LL}^{B,BA}$ and $D_{LL}^{E,Ozeke}$ at larger μ values. Note that Liu et al. (2016) calculated $D_{LL}^{E,Liu}$ only for the μ -range of $400 < \mu [\text{MeV/G}] < 4{,}000$ of electron, and we extrapolate $D_{LL}^{E,\text{Liu}}$ outside the covered the μ -range for the simulations. Recently, Mei et al. (2022) conducted a study to more carefully expand $D_{LL}^{E, {
m Liu}}$ to lower μ -range $10 < \mu$ [MeV/G] < 400. However, the D_{LL} results are not very different from what we achieved by the simple extrapolation and including the results from Mei et al. (2022) over the lower μ -range does not significantly change the DREAM3D simulation results. This similarly applies to the $D_{LL}^{E, \text{Liu}}$ at higher μ -range of 4,000 < μ [MeV/G] < 10^5 . By testing runs with DREAM3D, we find that its effects are also small on the electrons at the middle range of μ , over which we compare to the observations. Therefore, we choose to apply extrapolation over the μ -range not directly covered by the $D_{IL}^{E, \text{Liu}}$ model for the relevant simulations.

LEE ET AL. 12 of 20



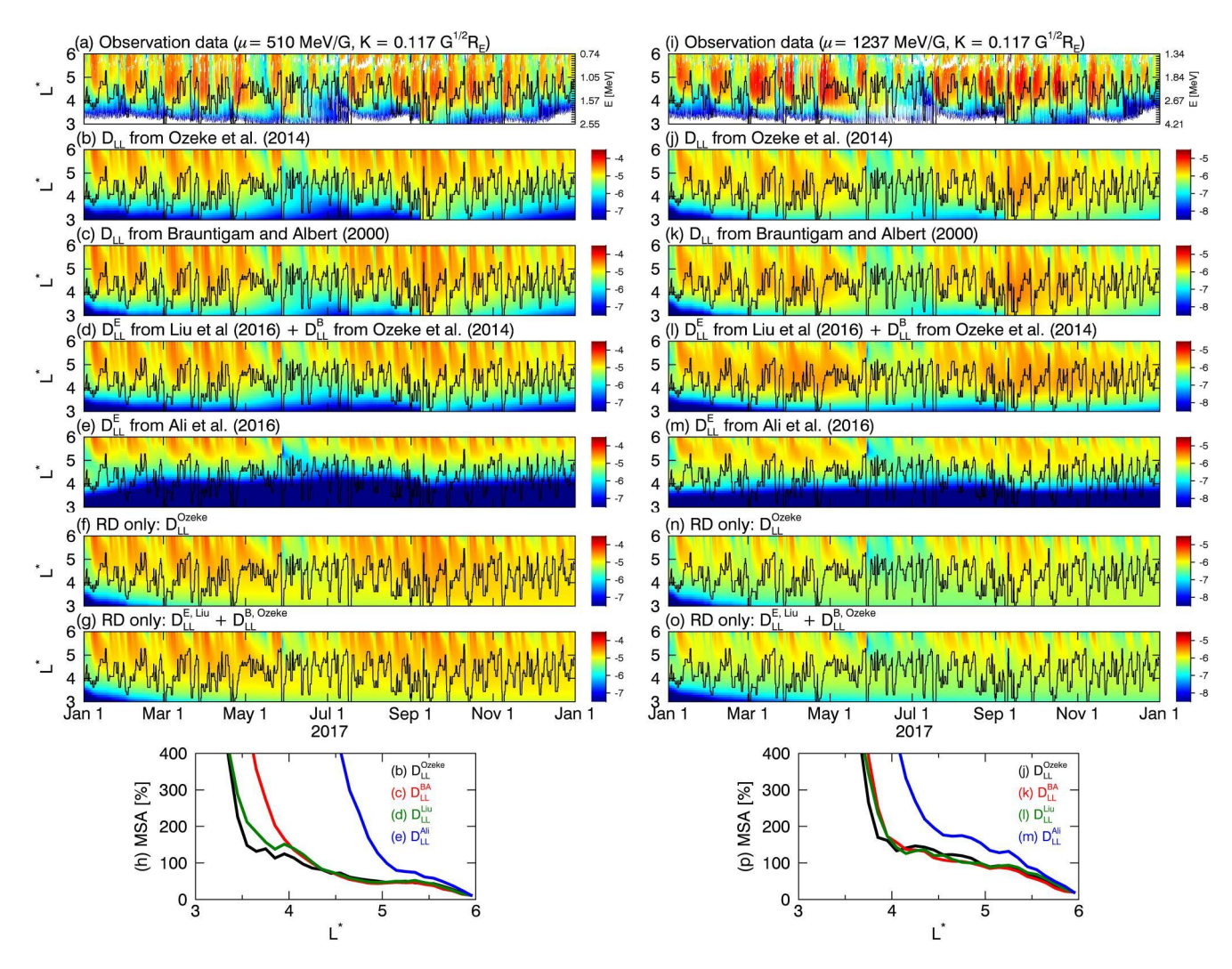


Figure 7. (a, b, i, j) Identical to Figures 1a, d and 1f, i, respectively. The remaining spectral plots are simulated phase space density with (c, j) D_{LL}^{BA} , (d, l) D_{LL}^{Liu} , and (e, m) D_{LL}^{Ali} , (f, n) D_{LL}^{Ozeke} but radial diffusion (RD) only, (g, o) D_{LL}^{Liu} but RD only. (h, p) The median symmetric accuracy distribution as a function of L^* .

Figure 7 shows the simulation results with the various RD coefficient input models. Figures 7b and 7j show the baseline cases with D_{LL}^{Ozeke} . Figures 7c and 7k show the simulated PSD variation with D_{LL}^{BA} , which are slightly larger than those with D_{LL}^{Ozeke} due to the slightly higher D_{LL} . Their overall performance is similar to D_{LL}^{Ozeke} at $L^* > 4$ as shown in the MSA results in Figures 7h and 7p (comparing the red to the black), while at lower L^* regions its performance is worse due to the larger overestimation. With the D_{II}^{liu} model, simulation results in Figure 71 show the highest values of PSD at large L^* regions during some enhancement periods (e.g., in May) compared to the other runs, especially at the higher μ value, even though $D_{LL}^{\rm Liu}$ could be smaller than $D_{LL}^{\rm Ozeke}$ and D_{LL}^{BA} at high μ values during active times (e.g., Figure 6b at Kp = 5). This is because D_{LL}^{Liu} has a strong μ dependence. Even though it is comparable to or even slightly smaller than D_{LL}^{Ozeke} at higher μ values, D_{LL}^{Liu} is higher than D_{IL}^{Ozeke} at lower μ values (e.g., Figure 6c), which could bring in more low-energy seed electrons from the outer boundary, enabling a higher level of local heating by chorus waves. To demonstrate this, we run the simulations with RD only using D_{LL}^{Ozeke} and D_{LL}^{Liu} respectively and show the simulation results in Figures 7f, 7g, 7n, and 70 (bottom two panels of each plot) for the two μ values. Comparing Figure 7f with Figure 7g (similarly Figure 7n with 70), we find that the RD only results with D_{LL}^{Liu} are quite similar to those with D_{LL}^{Ozeke} , suggesting that the more enhanced PSD values with D_{II}^{Liu} in the RD + Hiss + Chorus runs are from the stronger local heating by chorus waves due to higher supply of the seed electrons. Comparing the overall model performance using the MSA results in Figures 7h and 7p, we find that even though D_{LL}^{Liu} could lead to stronger enhancements of electron

LEE ET AL. 13 of 20

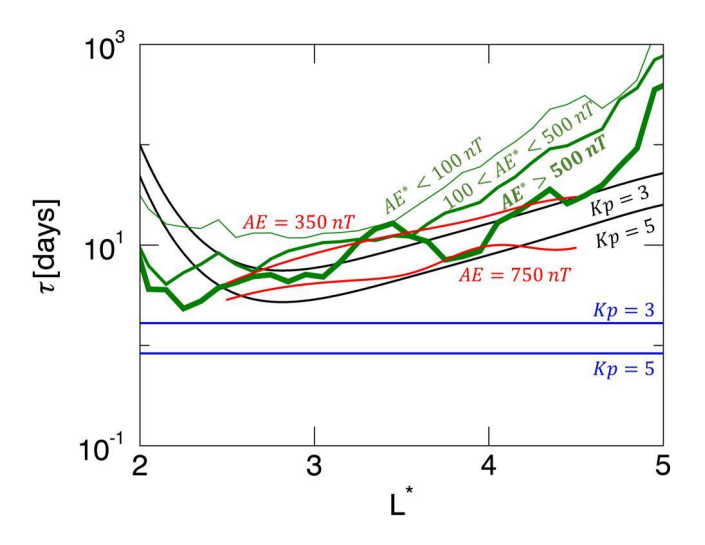


Figure 8. Electron lifetimes by hiss waves as a function of L^* of different models. The black curves show the lifetimes from Orlova et al. (2014) at Kp = 3 and 5 with the electron energy of E = 2 MeV. The red curves show the lifetimes from Agapitov et al. (2020) at different AE values at 350, and 750 nT with the same electron energy of E = 2 MeV. The green curves show the lifetime calculated using pitch angle diffusion coefficient ($D_{\alpha\alpha}$) by hiss wave from Tu et al. (2013) at three different AE* ranges. The blue lines show the simple lifetimes from Shprits et al. (2006) at different Kp values.

PSD, its overall performance at higher L^* regions (the green curves) is still comparable to that with $D_{LL}^{\rm Ozeke}$ (the black curves). But it results in more overestimation at 3.5 < L^* < 4 regions thus higher MSA there. Lastly, the simulation results with the $D_{LL}^{\rm Ali}$ model are plotted in Figures 7e and 7m, which show far limited values of PSD due to its smallest values of D_{LL} (e.g., Figure 6). The MSA results are also higher than the others (blue curves in Figures 7h and 7p). Therefore, the baseline simulation with $D_{LL}^{\rm Ozeke}$ overall shows the best performance over all the L^* regions.

The findings from our simulations with DREAM3D are similar to those from Drozdov et al. (2021) using the VERB3D code, in that the simulation results with D_{LL}^{BA} , D_{LL}^{Ozeke} , and D_{LL}^{Liu} result in similar levels of PSD variations, while the simulation results with D_{LL}^{Ali} show limited RD. However, it is hard to directly compare these DREAM3D results with the VERB results in Drozdov et al. (2021) since they are simulating different time intervals and the model performance is evaluated using different metrics. We use MSA here to compare the observed and modeled PSD over L^* , while Drozdov et al. (2021) adopted the normalized differences to compare the observed and modeled flux, which emphasize errors near peak flux values.

4.4. Hiss Wave Effect Models

In this subsection we investigate the effects of different input models of hiss waves. Examples of the estimated hiss loss lifetimes from the Orlova et al. (2014) model for 2 MeV electrons at different Kp values are shown in

Figure 8 versus L^* as the black curves, which show a strong L^* and Kp dependence. Similarly, the estimated lifetimes of 2 MeV electrons at different AE values from Agapitov et al. (2020) are shown in Figure 8 as the red curves, which show a different L^* dependence compared to that from the Orlova et al. (2014) model. The Kp and AE values in Figure 8 are selected to approximately compare the lifetimes from these two hiss models at similar geomagnetic activity levels. Based on the empirical relationship between Kp and AE suggested by Rostoker (1991), that is, AE(nT) = 200Kp-250, Kp = 3 roughly corresponds to the similar activity level as AE = 350 nT, and Kp = 5 roughly corresponds to AE = 750 nT. By comparing the black and red curves at $3 < L^* < 4$ (the region where hiss loss effects are most effective in the model), we find that the lifetimes from the Agapitov model (red curves) are longer than those from the Orlova model (black curves) at medium activity level (Kp = 3 and AE = 350 nT), while those lifetimes are generally comparable at higher activity level (Kp = 5 and AE = 750 nT). The lifetimes from Tu et al. (2013) are calculated from the pitch angle diffusion coefficient ($D_{\alpha\alpha}$) of hiss wave using Equations 12 and 13 of Lyons et al. (1972) and categorized at three different AE* ranges. The lifetime during the strong geomagnetic storm time (AE* > 500 nT), as depicted by the thick green curve, show fluctuations along L^* due to the insufficient data samples. Consequently, the lifetime is calculated to be longer than that during the intermediate storm time (100 < AE* < 500 nT) near $L^* \sim 3.3$.

In Figure 8 we also include a simple model of the electron lifetimes by hiss waves defined as $\tau = 5/\text{Kp}$ (Shprits et al., 2006), which are shown as the blue lines at the two Kp values, which have no energy or L^* dependence. We find the electron lifetimes from the simple model are the shortest among the three models illustrated.

Figure 9 shows the simulation results with the different electron loss models by hiss waves from Orlova et al. (2014), Agapitov et al. (2020), Tu et al. (2013), and Shprits et al. (2006), respectively. For low μ electrons, we find that the performance of the first three hiss loss models, Orlova et al. (2014), Agapitov et al. (2020), and Tu et al. (2013), are generally similar, with the Orlova et al. (2014) model producing slightly more loss at low L^* regions and thus a smaller MSA at $L^* < 4$ (comparing the black, red, and green curves in Figure 9f). This is consistent with the lifetime results shown in Figure 8 among these three models. For higher μ electrons, the MSA values from the three empirical models are almost identical as shown in Figure 9l. This is because the hiss scattering of higher energy electrons is limited in the model compared to the data, so that the small differences among the lifetime models do not significantly affect the results. Then, applying the simple lifetime model from Shprits et al. (2006) produces the strongest reduction of PSD inside the plasmasphere as shown in Figures 9e and 9k. This leads to the smallest MSA at $L^* < 3.7$ for the high μ case (blue curve in Figure 9l), but overestimates the

LEE ET AL. 14 of 20



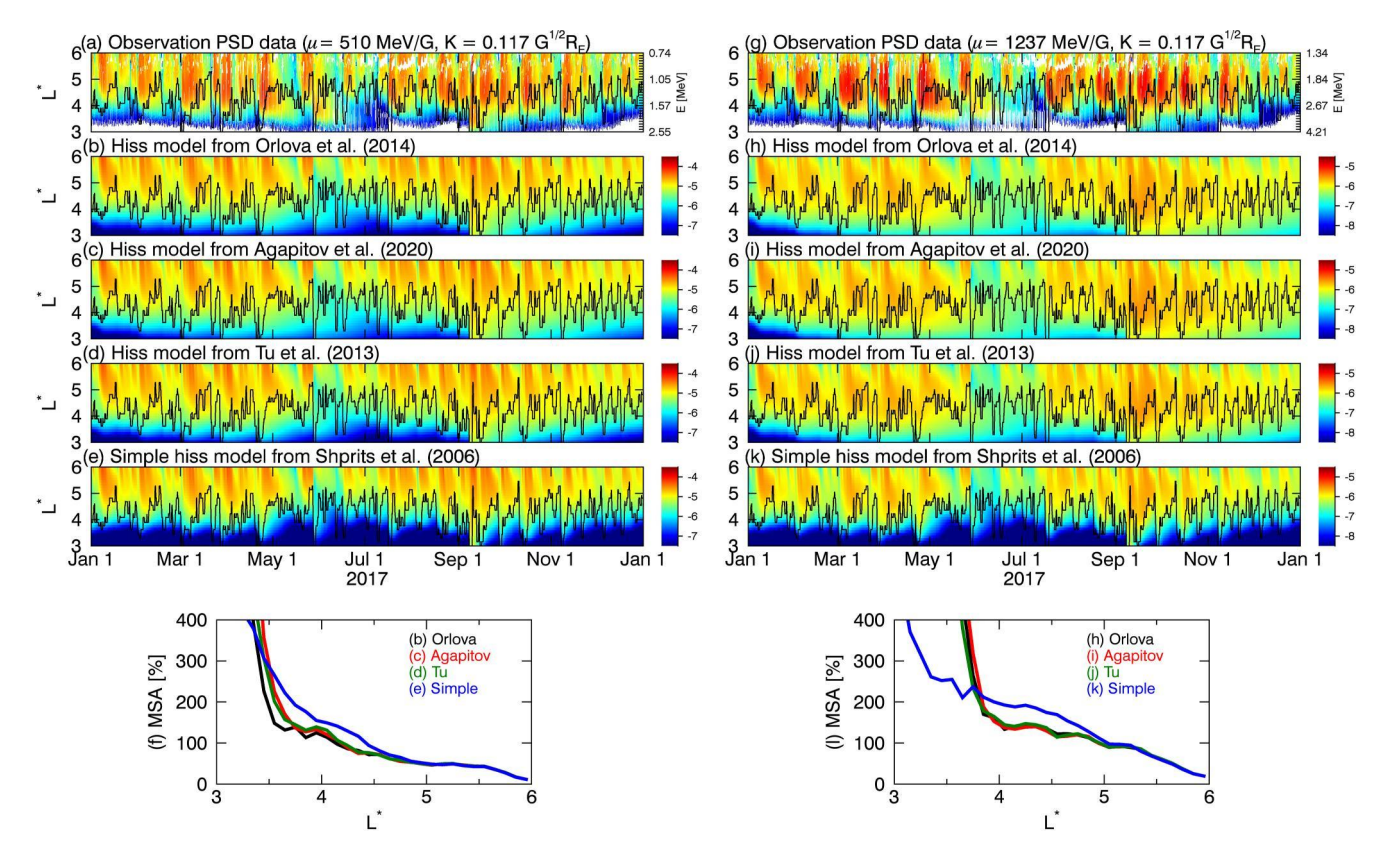


Figure 9. (a, b, g, h) Identical to Figures 1a, 1d, 1f, and 1i, respectively. The remaining spectral plots are simulated phase space density using the hiss model from (c, i) Agapitov et al. (2020), (d, j) Tu et al. (2013), and (e, k) Shprits et al. (2006). (f, l) The median symmetric accuracy and distribution as a function of L^* .

electron loss over medium L^* values, that is, $3.7 < L^* < 5$ for high μ (Figure 91) and $3.5 < L^* < 4.5$ for lower μ (Figure 9f). Even though the simple hiss loss lifetime model could produce better model performance at low L^* values, we don't implement it in our benchmark simulations since it is not as realistic as the other hiss loss models which are based on statistical wave data. However, these further suggest that stronger loss is needed near or inside the plasmapause to improve the model performance at low L^* regions.

4.5. Chorus Wave Models

At last, we investigate the effects of different chorus input models, the Wang et al. (2019) model based on the Van Allen Probes data and the Tu et al. (2013) model based on the CRRES data. Figure 10 compares the power of lower band chorus wave versus L^* , at different Kp values from Wang et al. (2019) in black curves, and at different AE* levels from Tu et al. (2013) in colored curves. We find that due to the different binning approaches, the chorus wave can reach higher power in Wang et al. (2019) at high Kp values than that from the AE-based model of Tu et al. (2013). Figure 11 shows the simulation results using the two different chorus wave models. We find the model performance to be very similar in the low μ case, with almost overlapping MSA values in Figure 11d. However, at high μ the results with the Tu et al. (2013) chorus model lead to less acceleration compared to the baseline case with the Wang et al. (2019) model, mainly because of the weaker wave power during active times from Tu et al. (2013) as shown in Figure 10. Correspondingly, the MSA comparison in Figure 11h shows that the error with the model from Wang et al. (2019) is smaller around the peak of the outer belt over $L^* = 4$ –5, but the error is higher at low L^* regions due to the increased level of overestimation.

5. Conclusions and Discussion

In this study, the DREAM3D diffusion model is applied to simulate the long-term radiation belt dynamics observed by Van Allen Probes and GOES over the entire year of 2017. We start with a benchmark simulation using the RD coefficients from Ozeke et al. (2014), the hiss wave model from Orlova et al. (2014), and the chorus

LEE ET AL. 15 of 20

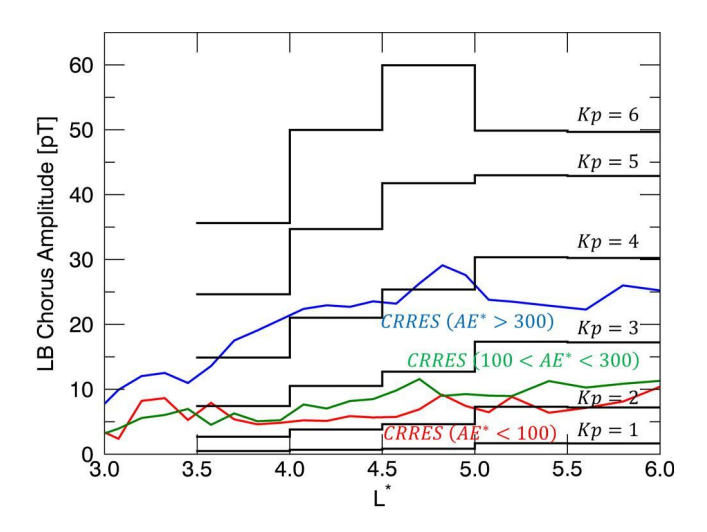


Figure 10. Black lines show the power of lower-band chorus waves at different Kp values versus L^* from Wang et al. (2019). The red, green and blue lines show the power of lower-band chorus waves at different AE ranges from the CRRES statistical wave model (Tu et al., 2013).

wave model from Wang et al. (2019), with the outer boundary condition driven by GOES data at $L^* = 6$. The benchmark simulations show that for the lower μ value of 510 MeV/G, RD can sufficiently transport the electrons inward from the data-driven outer boundary and hiss waves can lead to notable loss of electrons inside the plasmasphere even though faster loss rates are needed to reproduce the observations. Further adding in the chorus waves doesn't lead to apparent PSD enhancement at this μ value. Instead, it slightly reduced the electron PSD at low μ , improving the model performance at $L^* < 4.2$. On the other hand, the simulation results at higher μ value of 1237 MeV/G show different features than those at the lower μ value. Radial diffusion is shown to be insufficient in reproducing the electron enhancement at the higher μ value compared to the lower μ . Adding in chorus strongly improves the model performance at $L^* > 4$, suggesting that local heating by chorus waves plays a more dominant role compared to RD at the higher μ value. The overall model performance is worse at higher μ than lower μ , which suggests that both stronger chorus heating and faster electron loss near or inside the plasmapause are needed for higher energy electrons. In addition, some of the fast dropout of radiation belt electrons are not captured by the model, potentially due to the lack of EMIC waves, the uncertainty in the calculated LCDS using neural network, and nondipolar field effects associated with RD (Cunningham, 2016).

Then, using the benchmark simulation results as the baseline, we investigate the effects of various boundary conditions and model inputs on the performance of DREAM3D in reproducing the long-term outer belt dynamics. First, by testing the outer boundary conditions, we find that using the data-driven OB from the Van Allen Probes data at a lower $L^* = 5.5$ rather than that from the GOES data at $L^* = 6$ doesn't affect much the model performance at the lower μ value while greatly improves the performance at the higher μ value at $L^* > 4$ potentially due to the more dominant role of local heating at higher μ . However, using the open Neumann boundary condition at $L^* = 11$ significantly reduces the model performance. These demonstrate that energetic electron data from operational satellites like GOES are critical and generally sufficient to reproduce the global radiation belt dynamics inside the geosynchronous orbit over the long term. This is important for radiation belt nowcast and forecast and the relevant space weather applications.

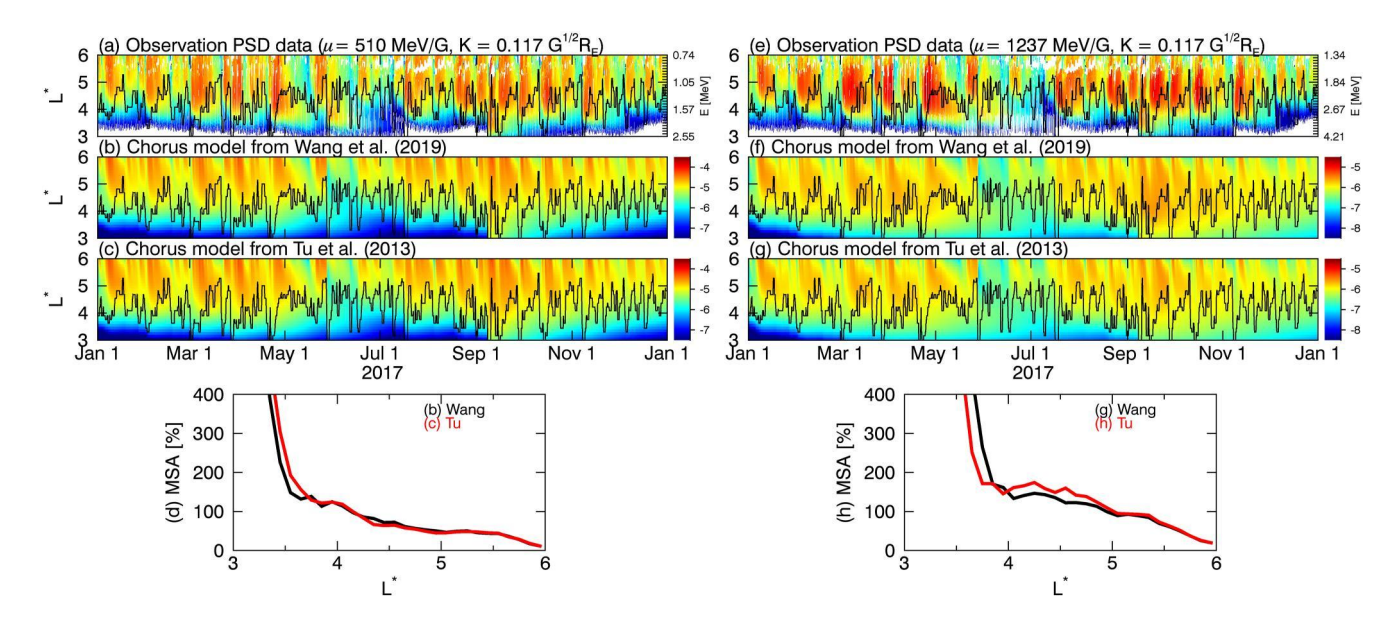


Figure 11. (a, b, e, f) Identical to Figures 1a, 1d, 1f, and 1i, respectively. (c, g) Simulated phase space density using CRRES statistical wave data for the chorus waves from Tu et al. (2013). (d, h) The median symmetric accuracy distribution as a function of L^* .

LEE ET AL. 16 of 20



Adding in the data-driven Emin BC for the seed electrons to the open Neumann boundary condition run improves the model performance but still performs poorly in reproducing the PSD enhancement at high L^* regions. Its overall performance is lower than the baseline run with data-driven OB condition, suggesting that the data-driven OB is more important in capturing the long-term dynamics of radiation belt electrons than the data-driven Emin BC. Then by adding in the data-driven Emin BC to the baseline run with the data-driven OB from GOES, we find that it does not improve the model performance. This seems counter-intuitive since one might expect the model performance to be improved by adding in more realistic data-driven boundary conditions.

One possible reason is explained in terms of the inward RD from the outer boundary condition. Low energy electrons (<100 keV) at the outer boundary are transported into lower L^* and are adiabatically energized as the background magnetic field increases. Then they reach the 100 keV threshold of the Emin BC at some L^* . In other words, the inward RD with the data-driven OB plays a similar role as the Emin BC. And the data-driven OB is not only including the electron injections from the plasma sheet, but also local heating at higher than the outer boundary location. Those are not included in the data-driven Emin BC. Also, the RD rates provided by the empirical D_{LL} models could be overestimated especially at low L^* regions and the loss from hiss waves inside the plasmasphere may be too slow, both of which will lead to overestimated PSD at low L^* . The observed dynamics of radiation belt electrons are a delicate balance among all these acceleration, transport, and loss processes. Making part of the inputs more realistic while keeping the others empirical may not necessarily improve the overall model performance. Please note that even though adding in the data-driven Emin BC doesn't improve the long-term performance of the simulations given that a data-driven OB is already in place, it could still improve the model performance during individual events, especially for those dominated by local acceleration as discussed in Tu et al. (2014).

The comparison between simulation results and observations in terms of MSA indicates that the model performances are always the best at the upper L-shell near the outer boundary when the data-driven outer boundary conditions are applied. While the inclusion of Emin BC does not enhance the performance when coupled with data-driven outer boundary conditions, it does enhance performance in the absence of such data-driven conditions. These suggest that to improve the nowcast and prediction of radiation belt dynamics, using physics-based, data assimilation, or machine learning models, it is necessary to include as much trustworthy data as possible.

The long-term simulation results are also sensitive to the input of RD coefficient. Overall, the simulation results with $D_{LL}^{\rm Ali}$ underestimate the observed electron PSD over a wide range of L, while the other three D_{LL} models, $D_{LL}^{\rm Ozeke}$, $D_{LL}^{\rm BA}$, and $D_{LL}^{\rm Liu}$ performed generally similarly at large L^* regions of $L^* > 4.3$. The best model performance at lower L^* regions is achieved in the baseline simulation with $D_{LL}^{\rm Ozeke}$. In addition, the strongly μ -dependent $D_{LL}^{\rm Liu}$ is shown to produce the most enhanced PSD from chorus heating especially at the higher μ , which is likely due to the higher supply of seed electrons by faster inward RD at low μ from the outer boundary.

We used the cold electron density model from Carpenter and Anderson (1992) for hiss wave inside the plasmasphere and the density model from Sheeley et al. (2001) for chorus waves outside the plasmasphere by following the previous work (Tu et al., 2013). The variation of cold plasma density strongly affects the diffusion coefficients in pitch angle and energy, and potentially contributes to the balance between acceleration and loss. In this reason, it is also important to investigate the various empirical models on cold electron density for the radiation belt dynamics, but we remain this work as a future work.

Testing the different input models of hiss and chorus waves, we find the model performance is generally similar using the hiss loss models from Orlova et al. (2014), Agapitov et al. (2020), and Tu et al. (2013), with a slightly better performance with Orlova et al. (2014) since its electron lifetimes are slightly shorter. Using the simple lifetime model from Shprits et al. (2006) produces the strongest reduction of PSD inside the plasmasphere and thus the smallest MSA at low L^* regions, which further suggests that stronger loss is needed near or inside the plasmapause, especially for higher-energy electrons. In fact, these losses of multi-MeV electrons could be more efficiently produced by EMIC wave scattering rather than hiss wave scattering. Recently, Drozdov et al. (2020) also show that hiss waves can aid EMIC waves in scattering the multi-MeV electrons inside the plasmasphere. Inclusion of the EMIC waves will be a future step in our DREAM3D simulations. From a different perspective, the simple hiss loss lifetime model from Shprits et al. (2006), despite being less realistic, could work the best for the purpose of radiation belt prediction.

LEE ET AL. 17 of 20



On the chorus wave input models, the Wang et al. (2019) model and Tu et al. (2013) model perform similarly for the low μ case. But the Wang et al. (2019) model performed better in producing the stronger electron enhancement at higher μ due to its higher chorus wave power during geomagnetic active times.

Data Availability Statement

Van Allen Probe HOPE, MagEIS, REPT data and the combined ECT level 3 data are available from the Science Operations and Data Center (https://rbsp-ect.newmexicoconsortium.org/rbsp_ect.php). Geomagnetic activity indices were obtained from the NASA OMNI Web (https://cdaweb.gsfc.nasa.gov/). The PSD data and simulation results presented in this study are publicly available at Zenodo (Lee et al., 2024).

Acknowledgments

This work was supported by the NASA Grants 80NSSC19M0146, 80NSSC21K1312, and 80NSSC21K2008, DOE Grant DE-SC0020294, and NSF Grant AGS 1752736. D. W. acknowledges the support from the DFG Grant WA 4323/5.1

References

- Agapitov, O., Mourenas, D., Artemyev, A., Claudepierre, S. G., Hospodarsky, G., & Bonnell, J. W. (2020). Lifetimes of relativistic electrons as determined from plasmaspheric hiss scattering rates statistics: Effects of ωpe/Ωce and wave frequency dependence on geomagnetic activity. Geophysical Research Letters, 47(13), e2020GL088052. https://doi.org/10.1029/2020GL088052
- Ali, A. F., Malaspina, D. M., Elkington, S. R., Jaynes, A. N., Chan, A. A., Wygant, J., & Kletzing, C. A. (2016). Electric and magnetic radial diffusion coefficients using the Van Allen probes data. *Journal of Geophysical Research: Space Physics*, 121(10), 9586–9607. https://doi.org/ 10.1002/2016JA023002
- Allison, H. J., & Shprits, Y. Y. (2020). Local heating of radiation belt electrons to ultra-relativistic energies. *Nature Communications*, 11, 4533. https://doi.org/10.1038/s41467-020-18053-z
- Aseev, N. A., & Shprits, Y. Y. (2019). Reanalysis of ring current electron phase space densities using Van Allen Probe observations, convection model, and log-normal Kalman filter. *Space Weather*, 17(4), 619–638. https://doi.org/10.1029/2018SW002110
- Aseev, N. A., Shprits, Y. Y., Drozdov, A. Y., & Kellerman, A. C. (2016). Numerical applications of the advective-diffusive codes for the inner magnetosphere. Space Weather, 14(11), 993–1010. https://doi.org/10.1002/2016SW001484
- Aseev, N. A., Shprits, Y. Y., Wang, D., Wygant, J., Drozdov, A. Y., Kellerman, A. C., & Reeves, G. D. (2019). Transport and loss of ring current electrons inside geosynchronous orbit during the 17 March 2013 storm. *Journal of Geophysical Research: Space Physics*, 124(2), 915–933. https://doi.org/10.1029/2018JA026031
- Brautigam, D. H., & Albert, J. M. (2000). Radial diffusion analysis of outer radiation belt electrons during the October 9, 1990, magnetic storm. Journal of Geophysical Research, 105(A1), 291–309, https://doi.org/10.1029/1999JA900344
- Carpenter, D. L., & Anderson, R. R. (1992). An ISEEE/whistler model of equatorial electron density in the magnetosphere. *Journal of Geophysical Research*, 97(A2), 1097–1108. https://doi.org/10.1029/91JA01548
- Cunningham, G. S. (2016). Radial diffusion of radiation belt particles in nondipolar magnetic fields. *Journal of Geophysical Research: Space Physics*, 121(6), 5149–5171. https://doi.org/10.1002/2015JA021981
- Drozdov, A. Y., Allison, H. J., Shprits, Y. Y., Elkington, S. R., & Aseev, N. A. (2021). A comparison of radial diffusion coefficients in 1-D and 3-D long-term radiation belt simulations. *Journal of Geophysical Research: Space Physics*, 126(8), e2020JA028707. https://doi.org/10.1029/2020JA028707
- Drozdov, A. Y., Shprits, Y. Y., Aseev, N. A., Kellerman, A. C., & Reeves, G. D. (2017a). Dependence of radiation belt simulations to assumed radial diffusion rates tested for two empirical models of radial transport. *Space Weather*, 15(1), 150–162. https://doi.org/10.1002/2016SW001426
- Drozdov, A. Y., Shprits, Y. Y., Orlova, K. G., Kellerman, A. C., Subbotin, D. A., Baker, D. N., et al. (2015). Energetic, relativistic, and ultra-relativistic electrons: Comparison of long-term VERB code simulations with Van Allen Probes measurements. *Journal of Geophysical Research: Space Physics*, 120(5), 3574–3587. https://doi.org/10.1002/2014JA020637
- Drozdov, A. Y., Shprits, Y. Y., Usanova, M. E., Aseev, N. A., Kellerman, A. C., & Zhu, H. (2017b). EMIC wave parameterization in the long-term VERB code simulation. *Journal of Geophysical Research: Space Physics*, 122(8), 8488–8501. https://doi.org/10.1002/2017JA024389
- Drozdov, A. Y., Usanova, M. E., Hudson, M. K., Allison, H. J., & Shprits, Y. Y. (2020). The role of hiss, chorus, and EMIC waves in the modeling of the dynamics of the multi-MeV radiation belt electrons. *Journal of Geophysical Research: Space Physics*, 125(9), e2020JA028282. https://doi.org/10.1029/2020JA028282
- Fälthammar, C.-G. (1965). Effects of time-dependent electric fields on geomagnetically trapped radiation. *Journal of Geophysical Research*, 70(11), 2503–2516. https://doi.org/10.1029/JZ070i011p02503
- Fei, Y., Chan, A. A., Elkington, S. R., & Wiltberger, M. J. (2006). Radial diffusion and MHD particle simulations of relativistic electron transport by ULF waves in the September 1998 storm. *Journal of Geophysical Research*, 111(A12), A12209. https://doi.org/10.1029/2005JA011211
- Fok, M.-C., Buzulukova, N. Y., Chen, S.-H., Glocer, A., Nagai, T., Valek, P., & Perez, J. D. (2014). The comprehensive inner magnetosphere-ionosphere model. *Journal of Geophysical Research: Space Physics*, 119(9), 7522–7540. https://doi.org/10.1002/2014JA020239
- Fu, H. S., Cao, J. B., Yang, B., & Lu, H. Y. (2011). Electron loss and acceleration during storm time: The contribution of wave-particle interaction, radial diffusion, and transport processes. *Journal of Geophysical Research*, 116(A10), A10210. https://doi.org/10.1029/2011JA016672
- Glauert, S. A., Horne, R. B., & Meredith, N. P. (2014a). Simulating the Earth's radiation belts: Internal acceleration and continuous losses to the magnetopause. *Journal of Geophysical Research: Space Physics*, 119(9), 7444–7463. https://doi.org/10.1002/2014JA020092
- Glauert, S. A., Horne, R. B., & Meredith, N. P. (2014b). Three-dimensional electron radiation belt simulations using the BAS Radiation Belt Model with new diffusion models for chorus, plasmaspheric hiss, and lightning-generated whistlers. *Journal of Geophysical Research: Space Physics*, 119(1), 268–289. https://doi.org/10.1002/2013JA019281
- Glauert, S. A., Horne, R. B., & Meredith, N. P. (2018). A 30-year simulation of the outer electron radiation belt. *Space Weather*, 16(10), 1498–1522. https://doi.org/10.1029/2018SW001981
- Kang, S.-B., Fok, M.-C., Komar, C., Glocer, A., Li, W., & Buzulukova, N. (2018). An energetic electron flux dropout due to magnetopause shadowing on 1 June 2013. *Journal of Geophysical Research: Space Physics*, 123(2), 1178–1190. https://doi.org/10.1002/2017JA024879
- Kim, K.-C., & Shprits, Y. (2013). Long-term relativistic radiation belt electron responses to GEM magnetic storms. *Journal of Atmospheric and Solar-Terrestrial Physics*, 100–101, 59–67. https://doi.org/10.1016/j.jastp.2013.04.007
- Kim, K.-C., Shprits, Y., Subbotin, D., & Ni, B. (2011). Understanding the dynamic evolution of the relativistic electron slot region including radial and pitch angle diffusion. *Journal of Geophysical Research*, 116(A10), A10214. https://doi.org/10.1029/2011JA016684

LEE ET AL. 18 of 20



- Kim, K.-C., Shprits, Y., Subbotin, D., & Ni, B. (2012). Relativistic radiation belt electron responses to GEM magnetic storms: Comparison of CRRES observations with 3-D VERB simulations. *Journal of Geophysical Research*, 117(A8), A08221. https://doi.org/10.1029/2011IA017460
- Kim, K.-C., Shprits, Y., & Wang, D. (2020). Quantifying the effect of plasmaspheric hiss on the electron loss from the slot region. *Journal of Geophysical Research: Space Physics*, 125(5), e2019JA027555. https://doi.org/10.1029/2019JA027555
- Lee, S.-Y., Tu, W., Cunningham, G. S., Cowee, M. M., Wang, D., Shprits, Y. Y., et al. (2024). Simulating long-term dynamics of radiation belt electrons using DREAM3D model [Dataset]. Zenodo. https://doi.org/10.5281/zenodo.7098603
- Lejosne, S., & Kollmann, P. (2020). Radiation belt radial diffusion at earth and beyond. Space Science Reviews, 216(1), 19. https://doi.org/10. 1007/s11214-020-0642-6
- Li, W., & Hudson, M. K. (2019). Earth's Van Allen radiation belts: From discovery to the Van Allen Probes era. *Journal of Geophysical Research:* Space Physics, 124(11), 8319–8351. https://doi.org/10.1029/2018JA025940
- Li, X. (2004). Variations of 0.7–6.0 MeV electrons at geosynchronous orbit as a function of solar wind. Space Weather, 2(3), S03006. https://doi.org/10.1029/2003SW000017
- Li, X., Schiller, Q., Blum, L., Califf, S., Zhao, H., Tu, W., et al. (2013). First results from CSSWE CubeSat: Characteristics of relativistic electrons in the near-earth environment during the October 2012 magnetic storms. *Journal of Geophysical Research: Space Physics*, 118(10), 6489–6499. https://doi.org/10.1002/2013JA019342
- Liu, W., Tu, W., Li, X., Sarris, T., Khotyaintsev, Y., Fu, H., et al. (2016). On the calculation of electric diffusion coefficient of radiation belt electrons with in situ electric field measurements by THEMIS. *Geophysical Research Letters*, 43(3), 1023–1030. https://doi.org/10.1002/2015GL067398
- Lyons, L. R., Thorne, R. M., & Kennel, C. F. (1972). Pitch-angle diffusion of radiation belt electrons within the plasmasphere. *Journal of Geophysical Research*, 77(19), 3455–3474. https://doi.org/10.1029/JA077i019p03455
- Mei, Y., Li, X., Zhao, H., Sarris, T., Khoo, L., Hogan, B., & O'Brien, D. (2022). On the energy-dependent deep penetration of radiation belt electrons. Poster presented at GEM Workshop.
- Meredith, N. P., Horne, R. B., Iles, R. H. A., Thorne, R. M., Heynderikx, D., & Anderson, R. R. (2002). Outer zone relativistic electron acceleration associated with substorm-enhanced whistler mode chorus. *Journal of Geophysical Research*, 107(A7), 1144. https://doi.org/10.1029/2001JA900146
- Morley, S. K., Brito, T. V., & Welling, D. T. (2018). Measures of model performance based on the log accuracy ratio. *Space Weather*, 16(1), 69–88. https://doi.org/10.1002/2017SW001669
- Mourenas, D., & Ripoll, J. F. (2012). Analytical estimates of quasi-linear diffusion coefficients and electron lifetimes in the inner radiation belt. *Journal of Geophysical Research*, 117(A1), A01204. https://doi.org/10.1029/2011JA016985
- Olifer, L., Mann, I. R., Ozeke, L. G., Rae, I. J., & Morley, S. K. (2019). On the relative strength of electric and magnetic ULF wave radial diffusion during the March 2015 geomagnetic storm. *Journal of Geophysical Research: Space Physics*, 124(4), 2569–2587. https://doi.org/10.1029/2018JA026348
- Orlova, K., Spasojevic, M., & Shprits, Y. (2014). Activity-dependent global model of electron loss inside the plasmasphere. *Geophysical Research Letters*, 41(11), 3744–3751. https://doi.org/10.1002/2014GL060100
- Ozeke, L. G., Mann, I. R., Murphy, K. R., Jonathan Rae, I., & Milling, D. K. (2014). Analytic expressions for ULF wave radiation belt radial diffusion coefficients. *Journal of Geophysical Research: Space Physics*, 119(3), 1587–1605. https://doi.org/10.1002/2013JA019204
- Pinto, V. A., Mourenas, D., Bortnik, J., Zhang, X.-J., Artemyev, A. V., Moya, P. S., & Lyons, L. R. (2019). Decay of ultrarelativistic remnant belt electrons through scattering by plasmaspheric hiss. *Journal of Geophysical Research: Space Physics*, 124(7), 5222–5233. https://doi.org/10.1029/2019JA026509
- Reeves, G. D., Chen, Y., Cunningham, G. S., Friedel, R. W. H., Henderson, M. G., Jordanova, V. K., et al. (2012). Dynamic radiation environment assimilation model: Dream. *Space Weather*, 10(3), S03006. https://doi.org/10.1029/2011SW000729
- Reeves, G. D., McAdams, K. L., Friedel, R. H. W., & O'Brien, T. P. (2003). Acceleration and loss of relativistic electrons during geomagnetic storms. *Geophysical Research Letters*, 30(10), 1529. https://doi.org/10.1029/2002GL016513
- Ripoll, J.-F., Claudepierre, S. G., Ukhorskiy, A. Y., Colpitts, C., Li, X., Fennell, J., & Crabtree, C. (2020). Particle dynamics in the Earth's radiation belts: Review of current research and open questions. *Journal of Geophysical Research: Space Physics*, 125(5), e2019JA026735. https://doi.org/10.1029/2019JA026735
- Roederer, J. G. (1970). Dynamics of geomagnetically trapped radiation. Springer.
- Rostoker, G. (1991). A quantitative relationship between AE and Kp. *Journal of Geophysical Research*, 96(A4), 5853–5857. https://doi.org/10. 1029/90JA02752
- Schulz, M., & Lanzerotti, L. (1974). Particle diffusion in the radiation belts. Springer.
- Selesnick, R. S., & Blake, J. B. (2000). On the source location of radiation belt relativistic electrons. *Journal of Geophysical Research*, 105(A2), 2607–2624. https://doi.org/10.1029/1999JA900445
- Sheeley, B., Moldwin, M., Rassoul, H., & Anderson, R. (2001). An empirical plasmasphere and trough density model: CRRES observations. Journal of Geophysical Research, 106(A11), 25631–25641. https://doi.org/10.1029/2000JA000286
- Shprits, Y. Y., Kellerman, A. C., Drozdov, A. Y., Spence, H. E., Reeves, G. D., & Baker, D. N. (2015). Combined convective and diffusive simulations: VERB-4D com-parison with 17 March 2013 Van Allen Probes observations. Geophysical Research Letters, 42(22), 9600–9608. https://doi.org/10.1002/2015GL065230
- Shprits, Y. Y., Subbotin, D., & Ni, B. (2009). Evolution of electron fluxes in the outer radiation belt computed with the VERB code. *Journal of Geophysical Research*, 114(A11), A11209. https://doi.org/10.1029/2008JA013784
- Shprits, Y. Y., Thorne, R. M., Friedel, R., Reeves, G. D., Fennell, J., Baker, D. N., & Kanekal, S. G. (2006). Outward radial diffusion driven by losses at magnetopause. *Journal of Geophysical Research*, 111(A11), A11214. https://doi.org/10.1029/2006JA011657
- Spasojevic, M., Shprits, Y. Y., & Orlova, K. (2015). Global empirical models of plasmaspheric hiss using Van Allen Probes. *Journal of Geophysical Research: Space Physics*, 120(12), 10370–10383. https://doi.org/10.1002/2015JA021803
- Subbotin, D. A., & Shprits, Y. Y. (2009). Three-dimensional modeling of the radiation belts using the Versatile Electron Radiation Belt (VERB) code. Space Weather, 7(10), S10001. https://doi.org/10.1029/2008SW000452
- Summers, D., Thorne, R. M., & Xiao, F. (1998). Relativistic theory of wave–particle resonant diffusion with application to electron acceleration in the magneto-sphere. *Journal of Geophysical Research*, 103(A9), 20487–20500. https://doi.org/10.1029/98ja01740
- Thorne, R. M. (2010). Radiation belt dynamics: The importance of wave–particle interactions. *Geophysical Research Letters*, 37(22), L22107. https://doi.org/10.1029/2010g1044990
- Tsyganenko, N. A., & Sitnov, M. I. (2005). Modeling the dynamics of the inner magnetosphere during strong geomagnetic storms. *Journal of Geophysical Research*, 110(A3), A03208. https://doi.org/10.1029/2004JA010798

LEE ET AL. 19 of 20



- Tu, W., Cunningham, G. S., Chen, Y., Henderson, M. G., Camporeale, E., & Reeves, G. D. (2013). Modeling radiation belt electron dynamics during GEM challenge intervals with the DREAM3D diffusion model. *Journal of Geophysical Research: Space Physics*, 118(10), 6197–6211. https://doi.org/10.1002/jgra.50560
- Tu, W., Cunningham, G. S., Chen, Y., Morley, S. K., Reeves, G. D., Blake, J. B., et al. (2014). Event-specific chorus wave and electron seed population models in DREAM3D using the Van Allen Probes. *Geophysical Research Letters*, 41(5), 1359–1366. https://doi.org/10.1002/2013GL058819
- Tu, W., Xiang, Z., & Morley, S. K. (2019). Modeling the magnetopause shadowing loss during the June 2015 dropout event. *Geophysical Research Letters*, 46(16), 9388–9396. https://doi.org/10.1029/2019GL084419
- Wang, D., & Shprits, Y. Y. (2019). On how high-latitude chorus waves tip the balance between acceleration and loss of relativistic electrons. Geophysical Research Letters, 46(14), 7945–7954. https://doi.org/10.1029/2019GL082681
- Wang, D., Shprits, Y. Y., Zhelavskaya, I. S., Agapitov, O. V., Drozdov, A. Y., & Aseev, N. A. (2019). Analytical chorus wave model derived from Van Allen Probe observations. *Journal of Geophysical Research: Space Physics, 124*(2), 1063–1084. https://doi.org/10.1029/2018JA026183
- Wang, D., Shprits, Y. Y., Zhelavskaya, I. S., Effenberger, F., Castillo, A., Drozdov, A. Y., et al. (2020). The effect of plasma boundaries on the dynamic evolution of relativistic radiation belt electrons. *Journal of Geophysical Research: Space Physics*, 125(5), e2019JA027422. https://doi.org/10.1029/2019JA027422
- Yu, Y., Koller, J., Zaharia, S., & Jordanova, V. (2012). L neural networks from different magnetic field models and their applicability. Space Weather, 10(2), S02014. https://doi.org/10.1029/2011SW000743

LEE ET AL. 20 of 20